AD_____

Award Number: DAMD17-00-1-0323

TITLE: Helical Electron Avoidance Radiation Therapy (HEART) for Breast Cancer Treatment

PRINCIPAL INVESTIGATOR: Lijun Ma, Ph.D.

CONTRACTING ORGANIZATION: University of Maryland
Baltimore, MD 21201

REPORT DATE: April 2005

TYPE OF REPORT: Final

PREPARED FOR: U.S. Army Medical Research and Materiel Command
Fort Detrick, Maryland 21702-5012

REPORT DOCUMENTATION PAGE

Form Approved
OMB No. 0704-0188

1. REPORT DATE	2. REPORT TYPE	3. DATES COVERED
01-04-2005	Final	1 Apr 2000 – 31 Mar 2005

4. TITLE AND SUBTITLE

Helical Electron Avoidance Radiation Therapy (HEART) for Breast Cancer Treatment

5a. CONTRACT NUMBER

5b. GRANT NUMBER
DAMD17-00-1-0323

5c. PROGRAM ELEMENT NUMBER

6. AUTHOR(S)

Lijun Ma, Ph.D.

5d. PROJECT NUMBER

5e. TASK NUMBER

5f. WORK UNIT NUMBER

7. PERFORMING ORGANIZATION NAME(S) AND ADDRESS(ES)

University of Maryland
Baltimore, MD 21201

8. PERFORMING ORGANIZATION REPORT NUMBER

9. SPONSORING / MONITORING AGENCY NAME(S) AND ADDRESS(ES)
U.S. Army Medical Research and Materiel Command
Fort Detrick, Maryland 21702-5012

10. SPONSOR/MONITOR'S ACRONYM(S)

11. SPONSOR/MONITOR'S REPORT NUMBER(S)

12. DISTRIBUTION / AVAILABILITY STATEMENT
Approved for Public Release; Distribution Unlimited

13. SUPPLEMENTARY NOTES

14. ABSTRACT

The goal of this project is to develop helical electron beams for radiation therapy ofbreast cancers. This final report summarizes major findings and results for the entireperiod of the project. The results are organized based on the Statement of Work in ourproposal. During the entire grant funding period, we completed and exceeded all the tasksoutlined in the original specific aims. In particular, we validated our hypothesis andcharacterized the dosimetric properties of helical electron beams modulated via axialmagnetic field. We published multiple articles reporting the key milestones of project.In addition, We are awarded a patent by the US patent office on the device and methods ofuse of the helical electron beams in radiation therapy. The grant had supported fourpostdoctoral fellows with two of them are currently holding faculty positions at theacademic institutions. Our on-going work in translating our research into clinicalpractices is currently funded through Susan G. Komen Breast Cancer foundation.

15. SUBJECT TERMS
Radiation Oncology, Radiation Dosimetry, Treatment Planning Electron, Computer Optimization, Magnetic Collimator

16. SECURITY CLASSIFICATION OF:			17. LIMITATION OF ABSTRACT	18. NUMBER OF PAGES	19a. NAME OF RESPONSIBLE PERSON
a. REPORT	b. ABSTRACT	c. THIS PAGE			19b. TELEPHONE NUMBER *(include area code)*
U	U	U	UU	31	

Table of Contents

Introduction

The goal of this project is directed at developing a new breast cancer radiation therapy technique using helical electrons generated via axial magnetic field. The specific aims of this study are (1) to develop tools for realizing helical electron beam deliveries, (2) to develop dose modeling methods for helical electron beams, and (3) to carry out verifications and measurements for characterizing helical electron beams. Our end point is to test the technical feasibilities of generating helical electrons and its applications for breast cancer treatments. We made two breakthroughs in this period: (1) we successfully generated and characterized the helical electrons (2) we developed and measured a new breast tumor bed irradiation technique using the helical electron beam.

Body of Report

Our major findings are described as follows:

Task 1. Develop beam delivery tools for HEART

We first carried out Monte Carlo calculations for the methods of generating helical electron beams. The purpose of the study is to seek methods of producing the helical electron beams and to validate the dosimetric properties of magnetically modulate electrons. The details of the study are given in the attached reprint article [Earl and Ma, 2001]. Our study found significant skin sparing effects and enhanced depth dose curves when using axial in-air magnetic collimations. One result is illustrated in the following Figure:

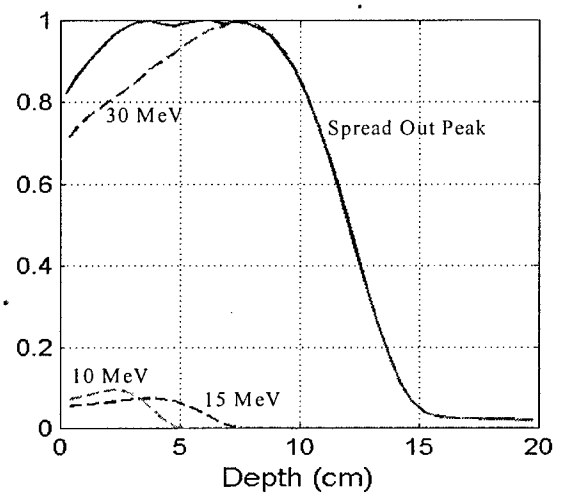

In the figure, we combined the magnetically collimated electrons of three different energies (30 MeV, 15 MeV and 10 MeV) and produced a spread-out enhanced depth dose peak ranging from the depth of 3 cm to 8 cm. This peak is analogous to the spread-out Bragg peak of the proton beam. The entrance dose for the spread-out peak is maintained at 80% of the maximum dose.

Based on the results of our theoretical calculations, we constructed a prototype axial magnetic collimator using Nd-Fe compound. The choice of permanent magnets is to eliminate bulky cooling and power supply assemblies associated with the superconducting and electromagnetic magnets. This enables the magnetic collimated directly attached to the end of standard electron cone and facilitate both fixed and rotational beam deliveries. The schematics of the deliveries are shown in Figure 2

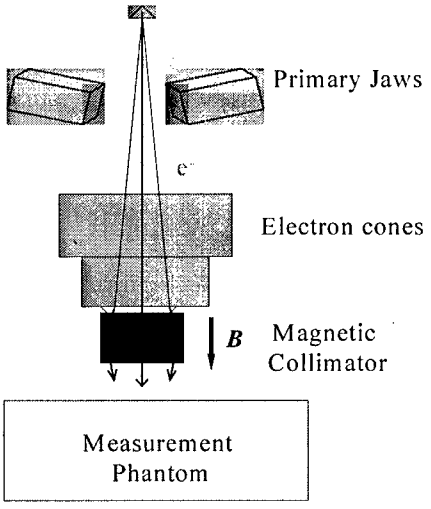

Shown in this figure are the beam transport and the delivery setup of a magnetic collimator. The electrons produced from the virtual source first pass through the primary jaws and then the tertiary electron cone. The axial magnetic field below the electron cone bends the electrons to follow a partial helical path. The net effect is reduced beam divergence thus the outward scattering effects. Based on our calculations, the magnetic field strength for 6 MeV electrons is approximately 0.5 T.

Task 2. Develop and implement optimized beam delivery methods for HEART

Following the theoretical calculations, we completed the design and commissioning of a prototype magnetic collimator. We further developed an extended pencil dose model for calculating the dose deposition of the magnetically collimated electron beams. The details of the model formalism and studies are given the attached reprint article [Phaisangittisakul, D'Souza and Ma, 2004]. As illustration, a simulated case is shown in the following Figure.

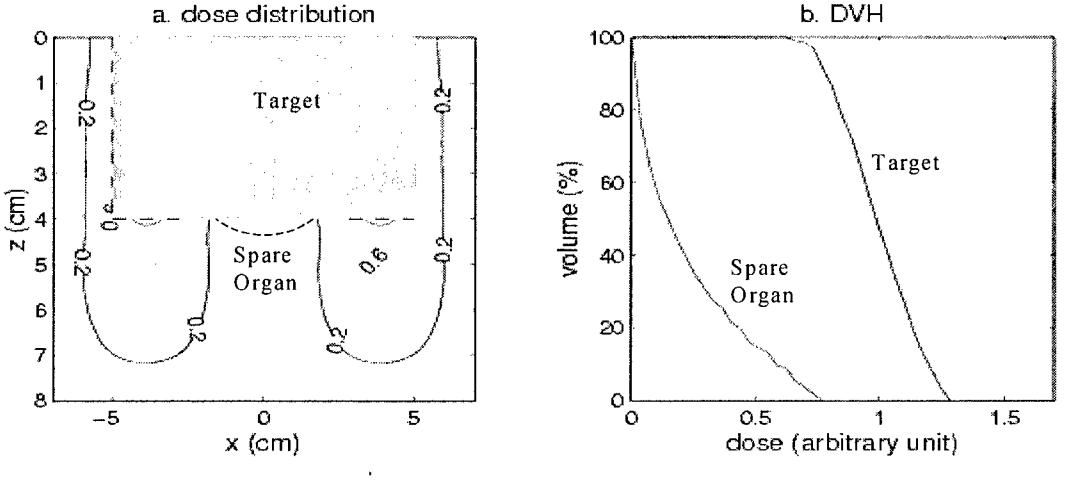

In this simulated case, several fixed enfaced helical electron beams are used to irradiate a superficial target volume while sparing the underlying normal tissue. Another important application of the helical electron beams is to irradiate the breast tumor bed using rotational arc beams. The results of the model calculated arc-beam delivery are shown in the following figure.

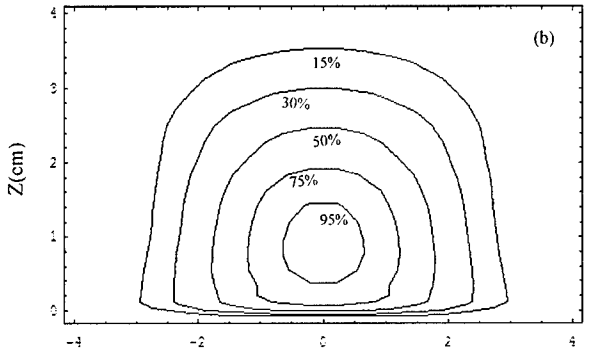

In this case, a single magnetically collimated electron arc beam (-40° to 40°) irradiates a flat phantom from posterior to anterior direction. One feature for such delivery is that significant skin-sparing effects are observed. To verify these results, we performed phantom measurements of the helical electron beams.

Task 3. Develop dose verification tools for HEART

We commissioned a cylindrical chest phantom made from tissue-equivalent materials. The phantom was used in the measurements of both fixed and rotational helical electron arc beam deliveries. The details of the study are given in the attached reprint article [Ma, 2004]. The comparison results of dose profile measurements and the depth dose curves of 9 MeV electrons with and without magnetic field collimation are illustrated in the following figure.

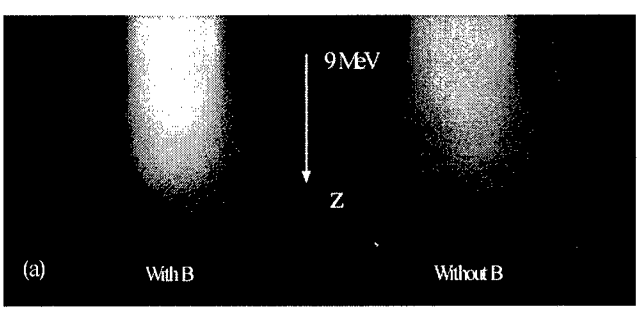

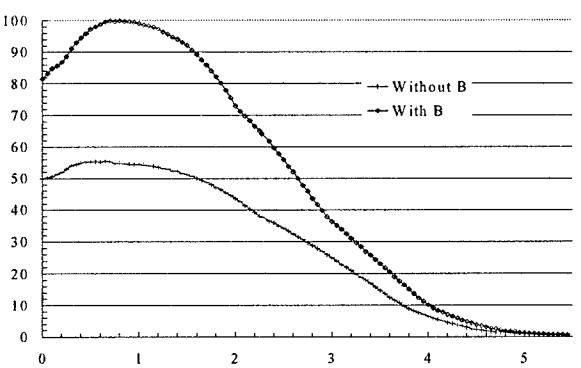

From the results of the measurements, we found that magnetically collimated electrons possess significantly higher dose deposition (>100%) than the conventional electrons. In contrast, the entrance dose for the magnetically collimated electron is on average 15% lower than that of the conventional electron beam.

Key Research Accomplishments

- We successfully generated magnetically collimated helical electron beams
- We developed a dose model for optimizing and calculating dose distributions of helical electron beams
- We characterized the dosimetric properties of fixed and rotational helical electron beams

List of Personnel Supported by the Grant

- Lijun Ma: Principal Investigator
- Matthew A Earl: Postdoctoral Fellow
- Nakorn Phaisangittisakul: Postdoctoral Fellow
- Allen X Li: Non-paying Consultant
- Kaile Li: Postdoctoral Fellow
- Mei Sun: Research Associate

Reportable Outcomes

(1) Refereed Papers

1. L. Ma, "Dosimetric properties of magnetically collimated electron beam for radiation therapy", Med. Phys. 31(11), 2973-2977, 2004.
2. K. Li, C. Yu and L. Ma "Improving a Scissor-Action Couch for Delivering Micro MLC-based Dynamic Arc Radiotherapy and Radiosurgery" Appl. Clin. Med. Phy. 5(3) 137-141, 2004.
3. K. Li, and L. Ma, "Selective Source Blocking for Treatment of Trigeminal Neuralgia Based on Analytical Gamma Knife Dose Modeling", Phys. Med. Biol. 49(15)3455-3463, 2004.
4. K Li, J Dai, and L. Ma, "Simultaneous minimizing monitor units and number of segments without leaf end abutment for segmental intensity modulated radiation therapy delivery", Med. Phys. 31(3)507-512, 2004.
5. N. Phaisangittisakul, W. D'Souza, and L. Ma, "Magnetic collimation and metal foil filtration for electron range and fluence modulation", Med. Phys. 31(1)17-23, 2004.
6. L. Ma, N. Phaisangittisakul, C. X. Yu and M. Sarfaraz, "A quality assurance method for verifying intensity modulated fields", Med. Phys, 30 (8) 2082-2088, 2003.
7. M Guerrero, XA Li, and L. Ma, "A technique to sharpen the beam penumbra for Gamma Knife Radiosurgery", Phys. Med. Biol. 48 1843-1853, 2003.
8. L. Ma, L.Chin, S. DiBiase, R. Gullapalli, A. Kennedy, and J Marc Simard, "Concomitant boost of stratified target volume with gamma knife radiosurgery: a treatment planning study", 26(4) 100-105e, Am. J. Clin. Oncol. 2003.
9. L. Ma, "Smoothing intensity-modulated treatment delivery under hardware constraints", Med. Phys. 29(12) 2937-2945, 2002.
10. N. Phaisangittisakul, and L. Ma, "An empirical model for independent dose verification of the Gamma Knife treatment planning", Med. Phys. 29(9) 1991-1997, 2002.

11. C.X. Yu, XA, Li, L. Ma, D, Chen, S. Naqvi, D. Shepard, M. Sarfaraz, T. Holmes, M. Suntharalingam and C. Mansfield, "Clinical implementation of intensity-modulated arc therapy", Int. J. Radiat. Oncol. Biol. Phys., 53(2) 453-463, 2002.
12. M. Earl and L. Ma, "Depth dose enhancement of electron beams subject to uniform longitudinal magnetic fields: a Monte Carlo study" Med. Phys., 29(4) 484-491, 2002.
13. L. Ma, C. Yu, M. Earl, T. Holmes, M. Sarfaraz, A. Li, D. Shepard, P. Amin, S. DiBiase, M. Suntharalingam and C. Mansfield "Optimized intensity modulated arc therapy for prostate cancer treatments", Int. J. Cancer /Rad. Oncol. Invest. Vol. 96 (6) 379-384, 2001.
14. L. Ma, L.Chin, S. DiBiase, R. Gullapalli, Richard Hudes, Andrew Kennedy, and J Marc Simard, "Concomitant boost of stratified target volume with gamma knife radiosurgery: a treatment planning study", in press, Int. J. Cancer/Radiat. Oncol. Invest. 2002.
15. X.A Li, L. Ma, S. Naqvi, R. Shih, and C. Yu, "Monte Carlo Dose Verification for Intensity Modulated Arc Therapy", Phys. Med. Biol. 46 No 9, 2269-2282. 2001.
16. L. Ma, "Minimizing field segments and leaf travel under hardware constraints for delivering intensity-modulated beam sequences", submitted, Phys. Med. Biol. 2001.
17. L. Ma, "Dependence of normal brain integral dose and Normal Tissue Complication Probability on the peripheral γ-knife prescription isodose values", Phys Med. Biol. 46(11) 3031-3041, 2001.
18. L. Chin, L, Ma, S. DiBiase, "Radiation Necrosis Following Gamma Knife Radiosurgery: A case-controlled comparison of Treatment parameters and long-term clinical follow-up", J. Neurosurgery, 94:899-904, 2001.
19. L. Ma, L. Chin, M. Sarfaraz, D. Shepard, and C. Yu, "An investigation of eye lens complication for gamma knife radiosurgery of trigeminal neuralgia" Appl. Clin. Med. Phy., Vol 1(4) 116-119, 2000.

(2) Major Presentations

1. The 4th Era of Hope Conference, Phildelphia, PA, 2005, US Department of Defense Breast Cancer Research Program.
2. The 2003 ASTRO Refresher Course, Salt Lake City, UT, ASTRO Annual Meeting Scientific Committee.
3. The 2002 ASTRO Refresher Course, New Orleans, LA, ASTRO Annual Meeting Scientific Committee.
4. Maryland BioScience Forums, Washington DC, 2001 & 2002, Sponsored by the Maryland BioAlliance, Techconcil, and the University of Maryland Systems

(3) Patent

L Ma, Helical Electron Beam Generating Device and Method of Use, US# 6,878,951

(4) Abstract

1. L. Ma, "Dosimetric properties of magnetically collimated electron beam for radiation therapy", Med. Phys. 31(2004) No. 6, 1797.
2. M. Guerrero, X.A. Li, L. Ma, J. Linder, C. DeYoung and B. Erickson," Simultaneous integrated IMRT boost for locally advanced gynecological cancers: Radiobiological and dosimetric considerations", Int. J. Rad. Oncol. Phys. Biol. 60(2004) No. 1, S482.

3. K. Li, and L. Ma, "Blocking plug pattern selection based on an automated critical region shielding (ACRS) algorithm fro Gamma Knife treatment planning", Med. Phys. 31(2004) No. 6, 1824.
4. L. Ma, and K. Li, " Selective source blocking for treatment of trigeminal neuralgia based on analytical Gamma Knife dose modeling", Med. Phys. 31(2004), No. 6, 1825.
5. K. Li, J. Dai, and L. Ma, "Eliminating leaf-end abutment while preserving the minimum number of segments and minimum monitor units for segmental IMRT delivery", Med. Phys. 31 (2004) No. 6, 1884.
6. L. Ma, M. Sarfaraz, C. Yu, "A statistical method for analyzing and verifying dynamic and static IMRT delivery", Med. Phys. 30 (2003) No. 6, 1417.
7. L. Ma, N Phaisangittisakul, W. D'Souza, "Use of magnetically collimated electrons and metal foil modulators for electron fluence and range modulation", Med. Phys 30 (2003) No. 6, 1446.
8. N. Phaisangittisakul and L. Ma, "Range-modulated electron radiotherapy with longitudinal magnetic field collimation", Med Phys 29 (2002) No. 6, 1287.
9. L. Ma, N. Phaisangittisakul, M. Sarfaraz and C. Yu "A machine-independent method for verifying rotational and fixed-beam intensity modulated radiation therapy", Med Phys 29 (2002) No. 6, 1366.
10. L. Ma, "Smoothing intensity modulated radiotherapy delivery under hardware constraints", Med Phys 29 (2002) No. 6, 1304.
11. N. Phaisangittisakul and L. Ma, "An empirical model for independent dose verification of the Gamma Knife Treatment Planning" Med Phys 29 (2002) No. 6, 1252.
12. L. Ma, M. Sarfaraz, S. DiBiase, and A. Kennedy, "A CT-based dose calculation method for intracavitary radiotherapy of GBM with GliaSite radioactive I125 filled catheter device", Radiology 207 (2002).
13. M. Earl, and L. Ma, "Characterization of helical electron beams for radiotherapy: a Monte Carlo study" Med. Phys. 28 (2001) No. 6, 1276.
14. L. Ma, D. Shepard and C Yu "An analytical dose model for treatment planning optimization and quality assurance of γ-knife stereotactic radiosurgery" Med. Phys. 28(2001) No. 6, 1255.
15. A. S. Kennedy, R. Murthy, M. Sarfaraz, C. Yu, B. Line, L. Ma and D. Van Echo, "Outpatient Hepatic Artery Brachytherapy for Primary and Secondary Hepatic Malignancies", Radiology 206 (2001).
16. L. Ma, C. Yu, M. Sarfaraz, T. Holmes, D. Shepard, A. Li, S. DiBiase, P. Amin, M. Suntharalingam, and C. Mansfield, "Simplified intensity modulated arc radiotherapy for prostate cancer treatments" Int. J. Rad. Oncol. 48 (2000) No. 3, 350.
17. X. A. Li, L. Ma, C. Yu, S. Naqvi, and T. Holmes, "Monte Carlo dose verification for intensity modulated ac therapy", Int. J. Rad. Oncol. 48(2000) No. 3, 219.
18. T. Holmes, D. Shepard, S. Naqvi, A. Li, L. Ma, and C. Yu, "Improvements to pencil beam-based inverse treatment planning methodology", Int. J. Rad. Oncol. 48 (2000) No. 3, 222.
19. C. Yu, X.A. Li, L. Ma, D. Shepard, M. Sarfaraz, T. Holmes, M. Suntharalingam, and C. Mansfield, "Clinical implementation of intensity modulated arc therapy", Int. J. Rad. Oncol. 48(2000) No. 3, 219.

Summary

The BC99087 project "Helical Electron Beam Avoidance Radiation Therapy for Breast Cancer Treatments" completed all the goals of the proposal. The key accomplishment is that we validated our hypothesis that magnetically modulated electron beams are beneficial in reducing excessive scatter and lower normal tissue dose for breast cancer radiation therapy. The results our studies allow us to pursue future studies in translating helical electrons into clinical practices.

Appendices

The following three articles are attached:

1. L. Ma, "Dosimetric properties of magnetically collimated electron beam for radiation therapy", Med. Phys. 31(11), 2973-2977, 2004.

2. N. Phaisangittisakul, W. D'Souza, and L. Ma, "Magnetic collimation and metal foil filtration for electron range and fluence modulation", Med. Phys. 31(1)17-23, 2004.

3.M. Earl, and L. Ma, "Characterization of helical electron beams for radiotherapy: a Monte Carlo study" Med. Phys. 28 (2001) No. 6, 1276.

APPENDIX 1

Dosimetric properties of magnetically collimated electron beams for radiation therapy

Lijun Ma[a)]
Department of Radiation Oncology, University of Maryland School of Medicine, Baltimore, Maryland 21201

(Received 12 December 2003; revised 18 August 2004; accepted for publication 31 August 2004)

A method of generating magnetically collimated electron beams is developed and the dosimetric properties of magnetically collimated electrons are investigated. An in-air magnetic collimator device was designed and constructed for the study. The magnetic collimator was placed above the exit port of a 14×14 cm^2 electron cone. Axial magnetic field of approximately 0.6 Tesla is generated inside the collimator via an array of permanent magnets. Fixed and rotational magnetically collimated electron beams were delivered and measured in phantoms. We found that magnetically collimated electron beams significantly lower the surface dose as compared with conventional electron beams. A magnetically collimated arc beam further reduces the surface dose to less than 20% of the maximum dose inside the target. The dose per monitor unit at d_{max} for the magnetically collimated electron beams was significantly (~40%) higher than that of the conventional electron beams. The use of magnetic collimation may lead to improved delivery techniques for breast and head and neck cancer treatments. © *2004 American Association of Physicists in Medicine.*
[DOI: 10.1118/1.1809780]

I. INTRODUCTION

Electrons are commonly used in radiation therapy for treating various cancers.[1–3] The excessive scattering of the existing cone-beam electrons often causes unwanted dose to the normal tissue contributing to the treatment-related toxicities such as telangiectasia, mucositis, and tissue fibrosis, etc. Early studies have indicated the benefits of using magnetic field to improve the dosimetric characteristics of the electron beams.[4–16]

In our previous studies, theoretical calculations of in-air magnetic collimation have shown significant reduction in the entrance dose of the electron beam and reduction in the depth dependence of the beam penumbra.[4,5] However, the question remains how to realize the magnetic field distribution for in-air magnetic collimation and how realistic delivery settings affect dosimetric properties of magnetically collimated electrons. In this study, we designed and constructed an in-air magnetic collimator and carried out beam-on measurements of magnetically collimated electron beams to study these questions.

The design of the magnetic collimator was based on the results derived from our previous studies.[4,5] The concept of using magnetic field dated back to 1950's by Bostick. The original idea was to apply a magnetic field inside the patient or the scattering medium to influence the scattered electrons inside the medium. Because the electrons can be constrained to a local area by a strong magnetic field, significant changes in the depth dose curve can be observed as the electrons gradually slow down. For example, a transverse magnetic field can be applied to the near end of the electron travel range to allow more energy deposited locally to generate an enhanced depth dose peak.[12] However, the difficulty of such in-medium application approach is that strong magnetic fields such as 10 T are needed as well as a large volume of the interaction or treatment area needs to be covered by the magnetic field.

In order to reduce excessive electron scattering, we applied an axial magnetic field in-air rather than in-media. The idea is to steer the electrons into a partial helical path before entering the downstream medium. This in effect compensates the divergence of the outward electron scattering inside the downstream medium. As a result, the magnetic field strength is significantly reduced by about an order of magnitude. In addition, the volume that needs to be covered by the magnetic field is also smaller when the field is applied in-air at a closer distance to the source than applied to the medium.

In this study, we constructed a magnetic collimator with approximately 0.6 T of axial magnetic field along its central axis. Beam-on measurements were carried out for 6–15 MeV electron beams. The goal of the study is to investigate the technical feasibility of in-air magnetic collimation and study the dosimetric properties of in-air magnetically collimated electron beams. We carried out the measurements of both fixed beam and arc beam deliveries with magnetically collimated electron beams. The dosimetric properties of magnetically collimated electron beams are also compared with those of conventional electron beams.

II. MATERIALS AND METHODS

The schematic of the experimental setup for the magnetically collimated electron delivery is given in Fig. 1. For our measurements, the magnetic collimator is placed near the end of the electron cone with an air gap of 5 cm from the isocenter. The setup of the magnetic collimator within the electron cone is shown in Fig. 2. The magnetic collimator is constructed from sintered Neodymium Iron Boron permanent magnets. The selection of permanent magnets instead of electromagnets and superconducting solenoids was for the

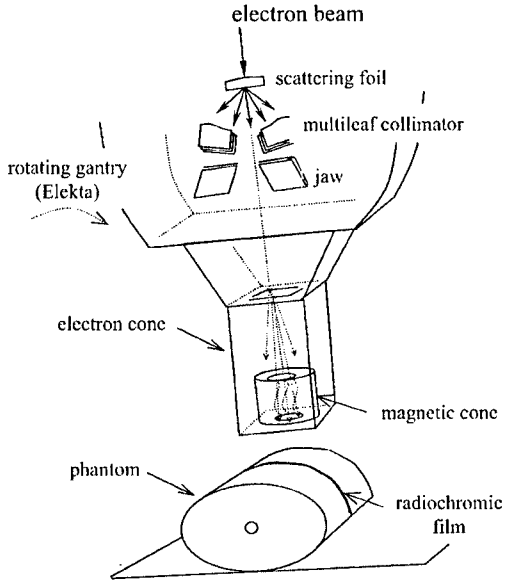

FIG. 1. The schematic of the beam delivery setup for the magnetically collimated electron beam.

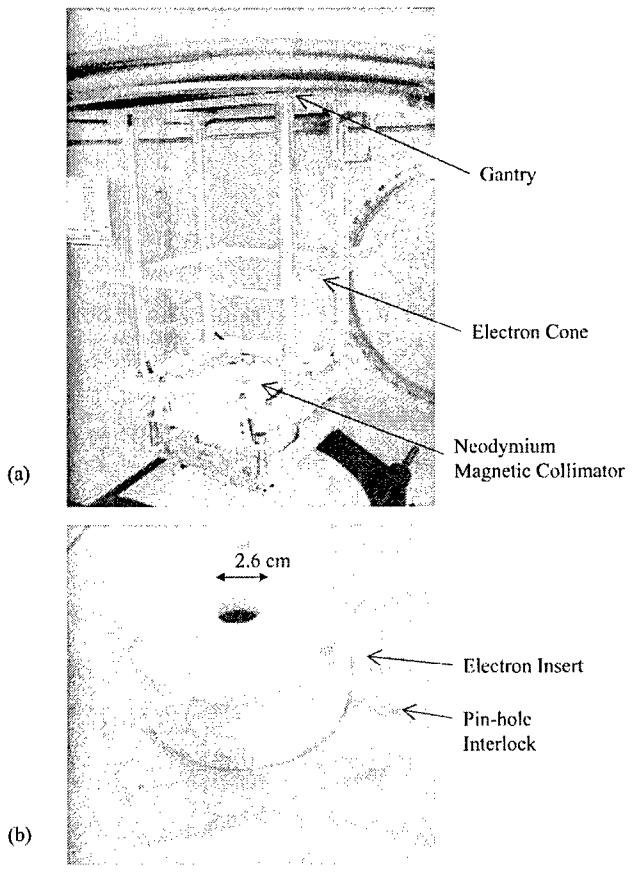

FIG. 2. Picture of an electron magnetic cone mounted on the electron cut-out attached to the electron cone of the Elekta SL20 linear accelerator: (a) Shows the set-up location of the magnetic collimator; (b) details the magnetic collimator and the custom made electron cut-out for mounting the magnetic collimator.

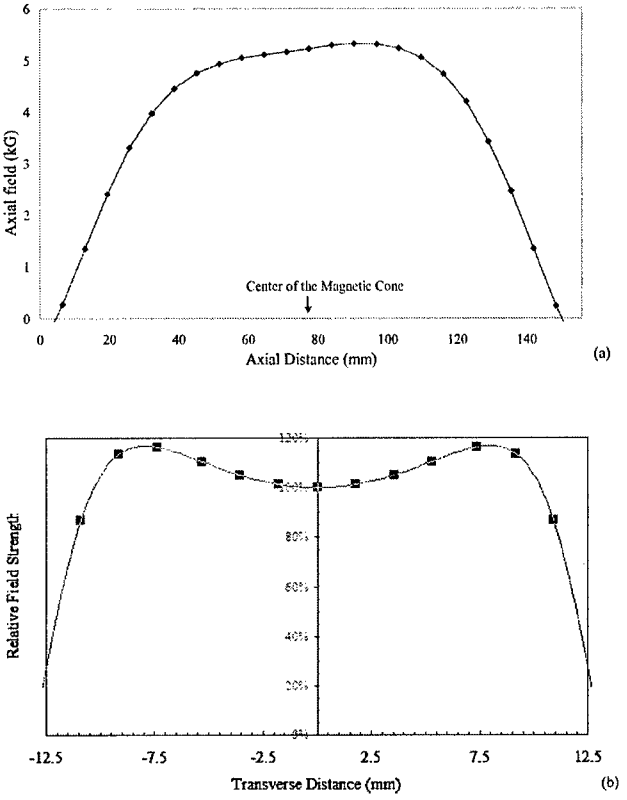

FIG. 3. The magnetic field distribution inside the magnetic collimator: (a) Is the cross sectional field distribution and (b) is the axial field distribution. The markers indicate measurement point and the solid line is the fitted curve.

ease of handling and no air–water cooling requirements for the permanent magnets. An aluminum/delrin shell was made to house the magnets to prevent charge buildup and reduce electron-induced changes inside the Neodymium compound. The magnetic collimator weighs approximately 3 kg. It has 2.6 cm inner diameter, 12.0 cm outer diameter, and a height of 8.0 cm. The magnetic collimator is attached to the 14 $\times$ 14 cm^2 electron cone with a locking plate near the exit port of the cone. The central axis of the magnetic collimator coincides with the electron cone. The magnetic collimator can be detached and mounted to the end of the electron cone without affecting the alignment and the positioning of the cone.

The magnetic field distribution inside and surround the magnetic collimator was measured using a pin-point Hall probe (Alpha Laboratory, Salt Lake City, UT). Axial and the transverse magnetic field distributions inside the collimator were measured by aligning the magnetic collimator with a bench ruler. The magnetic field distributions are shown in Fig. 3. The solid line for the transverse field profile of Fig. 3(a) was obtained using finite element analysis (Dexter Magnetics, Fremont, CA); the solid curve of Fig. 3(b) was interpolated based on the measurement data. Along the central axis, the maximum axial magnetic field was measured 0.6 T inside the collimator. The field strength increases from the

TABLE I. Summary of the surface dose and the relative beam output of magnetically collimated electrons in comparison with standard (std) electron beams.

Energy (MeV)	Surface dose relative to dose at d_{max}		Output at d_{max} (cCy/MU)		Practical range R_p (cm)		Mean range R_{50} (cm)	
	Magnetic	Std	Magnetic	Std	Magnetic	Std	Magnetic	Std
6	0.67	0.90	2.49	1.00	3.4	3.4	2.3	2.5
9	0.80	0.91	1.83	1.00	4.3	4.2	2.6	2.7
12	0.79	0.92	1.46	1.00	5.6	5.6	3.3	3.5
15	0.81	0.92	1.21	1.00	7.3	7.3	4.2	4.3

center towards the inner wall of the collimator. The strength of the peripheral maximum field is approximately 15% higher than that on the central axis.

We measured the percentage depth dose and the dose profiles of 6, 9, 12, and 15 MeV electrons beams through the magnetic collimator. The measurements were performed using radiographic films pressed between flat solid water blocks. In order to compare the dose profiles with those of conventional electron beams, we constructed a nonmagnetized metal collimator of the same geometry as that of the magnetic collimator. After each film exposure using the magnetically collimated electron beam, we swapped the magnetic collimator and the nonmagnetic collimator. The couch was then laterally shifted by approximately 5 cm and another area of the film was exposed to conventional electron beams. A 5 cm air gap was maintained between the end of electron cone and the phantom surface. Room lasers and optic distance readings were used to verify the position of the phantom and the alignment of the film between the two measurements. The two exposures were carried out with the same setups and the monitor units ranging from 70 to 100 MU.

When measuring the dose profiles of rotational arc-beam deliveries, we placed a radiographic film (EDR-2, Eastman Kodak, Rochester, NY) inside a cylindrical solid water phantom (Computerized Imaging Reference Systems, Norfolk, VA). The isocenter of the arc beam was placed at the d_{max} inside the solid water phantom. The cylindrical phantom has five metal fiducial markers that provided stereotactic registration of the isocenter positions and film alignment for the measurements. The electron arc beam was delivered from −40 degrees to +40 degrees. All exposed films were scanned using a 16-bit VidarPro film scanner with 0.08 mm resolution and analyzed with software (Radiological Imaging Technology, Colorado Springs, CO).

III. RESULTS

The depth dose characteristics of magnetically collimated electron beams as compared with conventional electron beams are summarized in Table I. A typical dose profile and the central axis depth dose curve for 9 MeV magnetically collimated electron beam are given in Fig. 4. In Fig. 4, the central axis depth dose curves are renormalized to its depth of the maximum dose for both magnetically collimated electron beam and conventional electron beam. The results of Table I and Fig. 4 show that the surface dose is approximately 15% smaller for the magnetically electron beams compared with the conventional electron beams of 6–15 MeV. However, the output for the magnetically collimated electron beams at d_{max} is on average 40% higher than that of conventional electron beams. This is illustrated in Fig. 4: The surface dose of 9 MeV magnetically collimated electron beam is 12% lower but the dose at d_{max} is 83% higher than the conventional electron beam. The mean range (R_{50}) and the practical range (R_p) of magnetically collimated electron beams agree within 2 mm of those of conventional electron beams. However, R_{50} of the magnetic collimated electron beams is on average smaller as compared with the conventional beam for all beam energies. This indicates that the

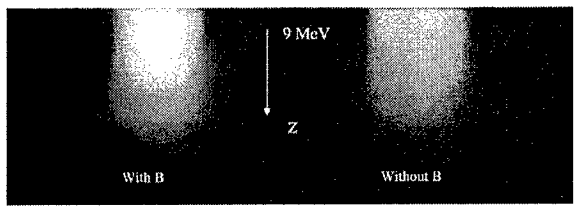

(a)

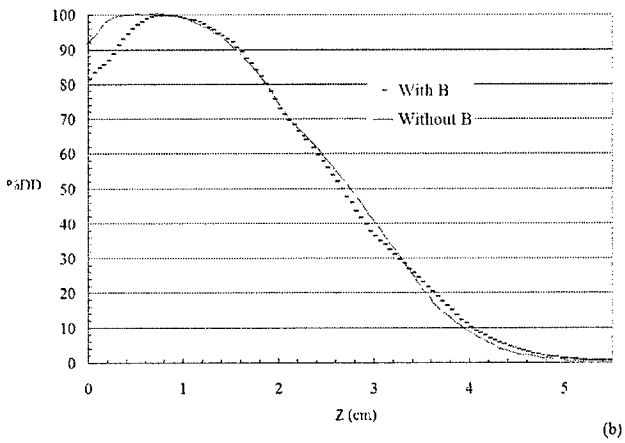

(b)

FIG. 4. Results of (a) two-dimensional dose distributions and (b) central axis depth dose curves of 9 MeV electrons with and without magnetic collimation. The magnetically collimated electron beam has higher dose per MU at d_{max}. The depth dose curve is renormalized to the d_{max} for both beams for comparison purposes.

TABLE II. Comparisons of the penumbra width of magnetically collimated electron beam with those of standard (std) electron beam.

	Penumbra width (20%–80%) at R_{90}		Penumbra width (20%–80%) at R_{50}		Penumbra width (40%–60%) at R_{90}		Penumbra width (40%–60%) at R_{50}	
Energy (MeV)	Magnetic (mm)	Std (mm)	Magnetic (mm)	Std (mm)	Magnetic (mm)	Std (mm)	Magnetic (mm)	Std (mm)
6	15.5	15.8	15.4	16.3	4.7	4.9	4.7	5.1
9	15.9	17.4	17.7	19.4	4.9	5.3	5.4	6.1
12	16.4	18.9	17.3	20.0	4.7	5.3	4.7	6.3
15	17.4	18.0	18.7	19.5	5.2	5.5	5.5	5.9

energy spectrum of magnetic collimated electron beams tend to shift towards the low energy side without affecting the maximum energy of the beam.

The depth dependence of the beam penumbra, i.e., 20%–80% width and 40%–60% width, for the increasing depths of R_{90} to R_{50} is summarized in Table II. The results of the 9 MeV magnetically collimated electrons are illustrated in Fig. 5. When analyzing the film, vertical profiles were extracted instead of the transverse profiles in order to minimize the background interferences between the two exposures. The measurements were repeated three to five times over a period of several months. The average values of measurements were shown in Table II. The 1σ deviations for the data are within 0.4 mm. From the results of Table II, the overall trend of the penumbra fall-offs for the magnetically collimated electron beams are faster than those of the conventional electron beams for all beam energies. The effects vary from 0.1 to 2.7 for different beam energies. The changes in the penumbra width from the depth R_{90} to R_{50} are also smaller for the magnetically collimated electron beams as compared with conventional electron beams. For example, the width of 40%–60% penumbra for the 12 MeV magnetically colli-

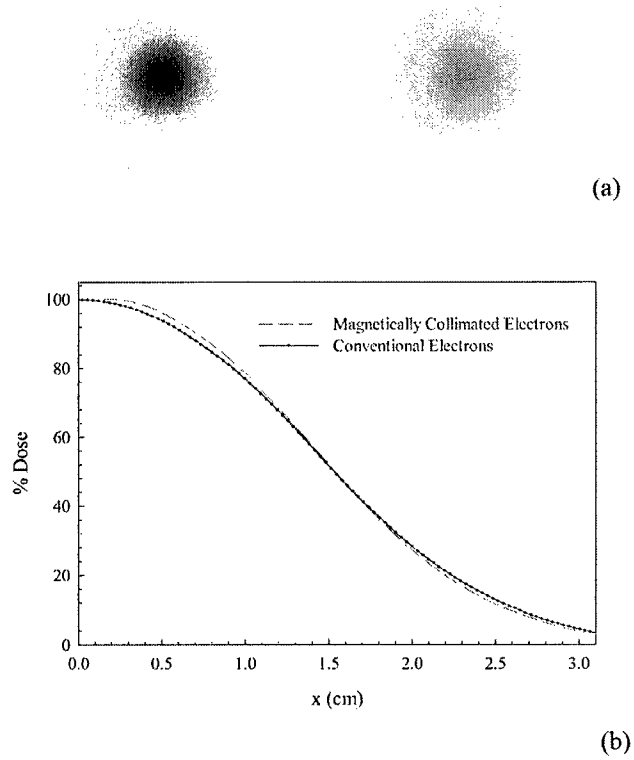

FIG. 5. Results of the two-dimensional dose profiles and penumbra fall-off at the depth of R_{50} for 9 MeV finite electron cone beam with and without magnetic collimation.

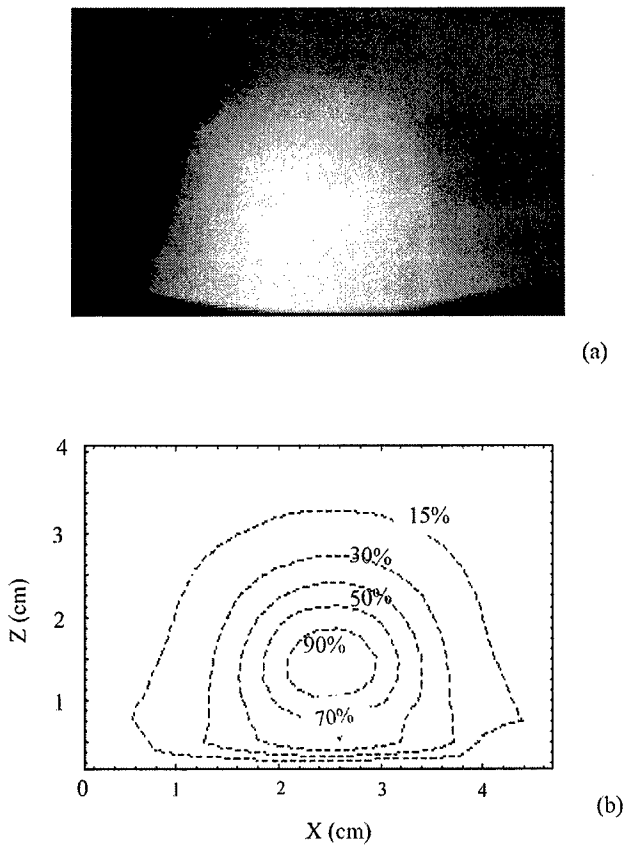

FIG. 6. The dose profile of magnetically collimated electron arc beam (9 MeV) measured inside a cylindrical water phantom. (a) Is the gray-scale film image, and (b) is the isodose distribution.

mated electron beam is the unchanged (4.7 mm) from R_{90} to R_{50}. However, it increases by 1.0 mm (from 5.3 to 6.3 mm) for the conventional electron beam.

Figure 6 shows the dose profile measured for the single arc delivery using a magnetically collimated electron beam. The electron arc beam was delivered with continuous dose rate during the gantry rotation. From the results of Fig. 6, the isodose surfaces particularly the high isodose surfaces such as 90% form concentric surfaces in the shape of ovoids. Figure 6 also shows significant skin-sparing effect, i.e., the surface dose was reduced to less than 20% of the maximum dose for the delivery.

IV. CONCLUSIONS

Magnetically collimated electron beams exhibit better skin-sparing effects over conventional electron beams. This result supports theoretical calculations of the previous studies. The dose per monitor units at the d_{max} was measured to be significantly higher for the magnetically collimated electron beams over the conventional electron beams. The penumbra fall-off was on average narrower for the magnetically collimated electron beams than for the conventional electron beams.

In general, the observed effects in the study are less pronounced in the measurements as compared with the theoretical calculations. Many factors may have contributed to these results: Suboptimal magnetic field distributions, dispersive beam energy spectra, limited field strength and restricted collimation sizes, etc. Our on-going studies include improving the technical aspects of the devices and perform detailed dose modeling of measurement data. Our future goal is to implement magnetically collimated electron beams for site-specific clinical studies.

ACKNOWLEDGMENTS

This work was supported by a research grant from U.S. Department of Defense Breast Cancer Research Program under Contract No. DAMD17-00-1-0323. The author thanks Dr. Warren D'Souza, Dr. Allen Li, Dr. Shaqid Naqvi, Dr. Mehrdad Sarfaraz, Dr. David Shepard, Dr. Xingen Wu, and Dr. Cedric Yu for support. Dr. Matthew Earl and Dr. Nakorn Phaisangittisakul carried out the initial calculations of the project. Mr. Weldon "Mac" McCready prepared the hardware for the measurements.

[a]Author to whom correspondence should be addressed. Telephone: (410) 328-7023. Electronic mail: lma@umm.edu

[1]K. R. Hogstrom, M. D. Mills, J. A. Meyer, J. R. Palta, D. E. Mellenberg, R. T. Meoz, and R. S. Fields, "Dosimetric evaluation of a pencil-beam algorithm for electrons employing a two-dimensional heterogeneity correction," Int. J. Radiat. Oncol., Biol., Phys. **10**, 561–569 (1984).
[2]D. D. Leavitt, L. M. Peacock, F. A. Gibbs, Jr., and J. R. Stewart, "Electron arc therapy: physical measurement and treatment planning techniques," Int. J. Radiat. Oncol., Biol., Phys. **11**, 987–999 (1985).
[3]F. M. Khan, "Basic physics of electron beam therapy," Front. Radiat. Ther. Oncol. **25**, 10–29 (1991).
[4]N. Phaisangittisakul, W. D'Souza, and L. Ma, "Magnetic collimation and metal foil filtration for electron range and fluence modulation," Med. Phys. **31**, 17–23 (2004).
[5]M. A. Earl and L. Ma, "Depth dose enhancement of electron beams subject to external uniform longitudinal magnetic fields: a Monte Carlo study," Med. Phys. **29**, 484–491 (2002).
[6]W. Bostick, "Possible techniques in direct-electron beam tumor therapy," Phys. Rev. **77**, 564–■ (1950).
[7]C. C. Shih, "High energy electron radiotherapy in a magnetic field," Med. Phys. **2**, 9–13 (1975).
[8]D. P. Whitmire, D. L. Bernard, M. D. Peterson, and J. A. Purdy, "Magnetic enhancement of electron dose distribution in a phantom," Med. Phys. **4**, 127–131 (1977).
[9]F. J. Farley, G. Fiorentini, and D. C. Stocks, "Influence of axial magnetic field on the multiple scattering of particle beams," Nucl. Instrum. Methods **152**, 353–356 (1978).
[10]R. Nath and R. J. Schulz, "Modification of electron-beam dose distributions by transverse magnetic fields," Med. Phys. **5**, 226–230 (1978).
[11]B. R. Paliwal, A. L. Wiley, Jr., B. W. Wessels, and M. C. Choi, "Magnetic field modification of electron-beam dose distributions in inhomogeneous media," Med. Phys. **5**, 404–408 (1978).
[12]M. S. Weinhous, R. Nath, and R. J. Schulz, "Enhancement of electron beam dose distributions by longitudinal magnetic fields: Monte Carlo simulations and magnet system optimization," Med. Phys. **12**, 598–603 (1985).
[13]A. F. Bielajew, "The effect of strong longitudinal magnetic fields on dose deposition from electron and photon beams," Med. Phys. **20**, 1171–1179 (1993).
[14]M. C. Lee and C. M. Ma, "Monte Carlo characterization of clinical electron beams in transverse magnetic fields," Phys. Med. Biol. **45**, 2947–2967 (2000).
[15]V. Y. Kuperman, "Electron beam transport in the presence of a strong, axial magnetic field," Med. Phys. **28**, 2522–2526 (2001).
[16]D. W. Litzenberg, B. A. Fraass, D. L. McShan, T. W. O'Donnell, D. A. Roberts, F. D. Becchetti, A. F. Bielajew, and J. M. Moran, "An apparatus for applying strong longitudinal magnetic fields to clinical photon and electron beams," Phys. Med. Biol. **46**, N105–N115 (2001).

Magnetic collimation and metal foil filtering for electron range and fluence modulation

N. Phaisangittisakul, W. D. D'Souza, and Lijun Ma[a)]
Department of Radiation Oncology, University of Maryland School of Medicine, Baltimore, Maryland 21201

(Received 14 March 2003; revised 8 September 2003; accepted for publication 8 October 2003; published 8 December 2003)

We investigated the use of magnetically collimated electron beams together with metal filters for electron fluence and range modulation. A longitudinal magnetic field collimation method was developed to reduce skin dose and to improve the electron beam penumbra. Thin metal foils were used to adjust the energies of magnetically collimated electrons. The effects for different types of foils such as Al, Be, Cu, Pb, and Ti were studied using Monte Carlo calculations. An empirical pencil beam dose calculation model was developed to calculate electron dose distributions under magnetic collimation and foil modulation. An optimization method was developed to produce conformal dose distributions for simulated targets such as a horseshoe-shaped target. Our results show that it is possible to produce an electron depth dose enhancement peak using similar techniques of producing a spread-out Bragg peak. In conclusion, our study demonstrates new aspects of using magnetic collimation and foil filtration for producing fluence and range modulated electron dose distributions. © *2004 American Association of Physicists in Medicine.*
[DOI: 10.1118/1.1630491]

I. INTRODUCTION

Excessive scattering is a significant problem for conventional electron beams. Due to scattering, the penumbra of an electron beam broadens as the depth increases. Therefore, overlapping or abutting electron fields are rarely used due to high dose inhomogeneity in the junction areas. As a result, a single-field setup is the standard technique for most electron beam applications in radiation therapy. In a previous study, we reported using enface longitudinal magnetic fields to reduce electron beam broadening effects and improve electron depth dose characteristics.[1] The key finding of our study was that the magnetic field could be applied in-air that is external to a scattering medium to produce skin sparing or depth dose enhancement effects. Since the in-air magnetic field bends the peripheral electrons toward the central beam axis via a partial helical path, only the trajectories of the primary electrons are modified without affecting the scattering condition of the secondary electrons. This approach is different from the early studies where the magnetic fields are used to improve the scattering condition of the secondary electrons.[2–12]

In this study, we investigated the use of magnetically collimated electrons in conjunction with filtering foils to produce range and fluence modulated electron dose distributions. In this method, we combine multiple electron pencil beams collimated via magnetic field and simultaneously vary the attenuating foils to produce conformal dose distributions. The use of multiple layers of metal foils for range modulation is analogous to range modulation techniques in proton therapy.[9,10] We developed a pencil beam dose model for computing and optimizing the electron dose distributions. The method was implemented for simplified cases with simulated target shapes. We also investigated the capability of generating a spread-out depth dose enhancement peak with magnetically collimated electrons.

This article is organized as follows: Sec. II describes methods of using filtered foils with magnetically collimated electrons. The formalisms are given for the pencil dose model and related dose optimization schemes. Section III shows the results of depth dose curves, isodose distributions, and dose volume histograms for treatment cases with simulated target shapes. The interpretation of the results is included. Section IV concludes our study.

II. MATERIALS AND METHODS

Electron beams were collimated using a magnetic collimator producing uniform longitudinal field. The effects of magnetic field collimation on the electrons was simulated using EGS4 Monte Carlo program with DOSXYZ that included tracking algorithms for electrons under electromagnetic fields.[1] The collimator is 12 cm in length with the smallest field opening being 3×3 cm^2 and the largest field opening being 10×10 cm^2. The maximum magnetic field strength is 2.0 T based on the geometry of a magnet collimator made from magnetized neodymium compound. We select the permanent neodymium magnet for its compact size and no requirements of air and watering cooling. Additionally, the cost of the permanent magnet is low compared with electromagnetic coils and superconducting systems. For our calculation, an electron virtual source was used. The source is set at 80 cm from the top surface of the magnetic collimator. The magnetic collimator is placed immediately at the end of the standard electron cone. A flat-surface water-equivalent phantom was placed below the magnetic collimator with an air gap of 10 cm to score the electron dose deposition. Metal foils of selected thickness were placed on the top surface of the magnetic collimator. The energy cut-off for electrons and photons in the Monte Carlo calculations was set to be 560 and 10 keV, respectively.

TABLE I. Typical field strength of an external magnetic collimator (12 cm long) for electron beams of a linear accelerator.

T (MeV)	B (T)
6	0.6
9	0.9
12	1.1
15	1.4
18	1.7
20	1.8

We investigated the effects of different metal foil filters for fluence and range modulation in conjunction with the magnetic collimation. The metal foils included aluminum (Al), beryllium (Be), copper (Cu), lead (Pb), and titanium (Ti). The foil ranged from 0.01 to 0.2 cm in thickness. The nominal energies for electron beams included 9, 12, 15, and 18 MeV, which falls within the range of 4–20 MeV of standard linear accelerators. Since the entrance electron beam energy determines the maximum depth of beam penetration, the metal foils are capable of adjusting the beam range from zero to the maximum depth.

Theoretically, an electron traveling through a magnetic field inside the collimator follows a helical path. The relationship between the kinetic energy (T), the number of helical rotations (N_{rot}), field strength ($|\vec{B}|$), and field's length (d) is given as

$$N_{\text{rot}} \approx 0.93 \times \frac{|\vec{\mathbf{B}}|\mathbf{d}}{1+2\mathbf{T}}, \tag{1}$$

where the field strength $|\vec{B}|$ is in tesla, the collimator length $\mathbf{d}$ is in centimeters, and the electron energy $\mathbf{T}$ is in MeV. If we set $N_{\text{rot}}=0.5$ for proper dose enhancement,[1] we can derive the relationship between the corresponding magnetic field strengths for commonly available electron beam energies. This is given in Table I. From the results of Table I, the magnetic field strength for in-air application is practically reachable using permanent neodymium magnets.

In order to optimize the modulated dose distributions, we developed an analytical pencil beam dose model that calculates the dose distributions of the electrons under the influence of magnetic collimator and metal foil filters. The formalism of this model is as follows:

$$D(x,y,z) = \int\int f(x-x',y-y',z) \times k(x',y',z) p(z) \times \left(\frac{\text{SSD}+d_{\max}}{\text{SSD}+z}\right)^2 dx'\,dy', \tag{2}$$

where $D(x,y,z)$ is the dose profile at depth z, f is the open beam fluence distribution, k is the kernel function, $p(z)$ is the central axis depth dose distribution, SSD is the source to skin distance, and $d_{\max}$ is the reference depth taken to be the depth of maximum dose for conventional electron beams. Equation (2) follows the similar formula of the electron pencil beam dose model except the effects of magnetic field are included in the kernel function k and depth dose function $p(z)$.

Since the magnetic collimator is symmetric in the x and y dimensions, we further reduced Eq. (2) into a two-dimensional form. We also expanded the kernel function into a linear combination of Gaussian functions. We neglected the beam transmission outside the opening of the magnetic collimator, the transmission function through the collimator was specified as a step function that assumes a value of one for the opening area and zero otherwise. This function is specified at the end of the magnetic collimator where $z=0$. Therefore, Eq. (2) is reduced to

$$D(x,z) = \frac{1}{2}\left[\text{erf}\left(\frac{w(z)-x}{\sigma(z)}\right) + \text{erf}\left(\frac{w(z)+x}{\sigma(z)}\right)\right] p(z) \times \left(\frac{\text{SSD}+d_{\max}}{\text{SSD}+z}\right)^2, \tag{3}$$

where erf is the error function, and w is half the field width as measured from the central axis to the 50% isodose line. Note that both $w(z)$ and $\sigma(z)$ are z-dependent functions where $\sigma(z)$ accounts for the effects of magnetic collimation, beam divergence, and angular scattering. Both $\sigma(z)$ and $w(z)$ are monotonically increasing functions.

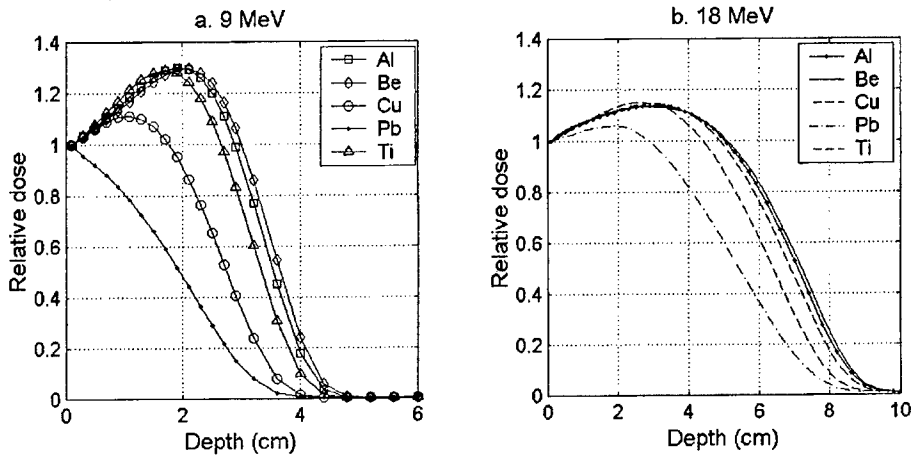

FIG. 1. Depth dose curves for 9 and 18 MeV electron beams with and without magnetic collimation. The effects of metal foils of different types are given.

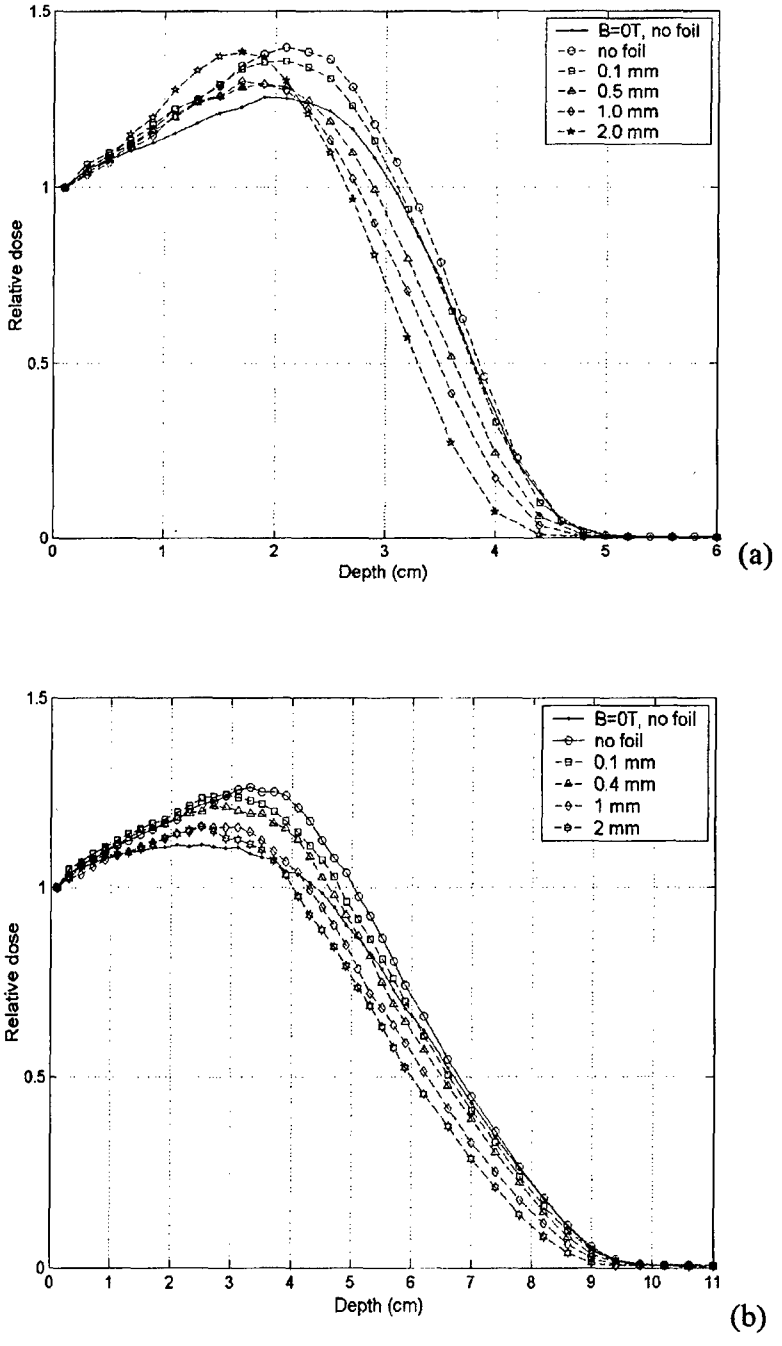

FIG. 2. Central-axis depth dose curves for 9 MeV (a) and 18 MeV (b) magnetically collimated electrons attenuated by Al foils as compared with the conventional electron beams.

In this study, we empirically determined $\sigma(z)$ and $w(z)$ along the z direction by fitting the pencil beam dose profiles (with a resolution of 0.3 cm) calculated using the Monte Carlo methods. These parameters were determined up to the depth where the central-axis percent depth dose reaches the bremsstrahlung tail of the depth dose curve (<3%). The parameters at other depths were interpolated using the cubic spline method.

The advantage of this dose model is that the cumulative dose function is in analytical form, which allowed us to directly compute the dose gradient. This facilitates the incorporation of dose optimization parameters such as the relative beam weights, position of the beam, and foil thickness for iterative calculations.

The objective function **O** for the optimization is given as follows:

$$\mathbf{O}=\sum_i \left[\sum_k \mathbf{w}_k \times \mathbf{D}_T(x_i-x_k,z_i)-\mathbf{D}_0\right]^2 + \alpha \sum_k \mathbf{w}_k \times \mathbf{D}_N(x_i-x_k,z_i), \quad (4)$$

where D_0 is the prescription dose value, D_T is the dose to the

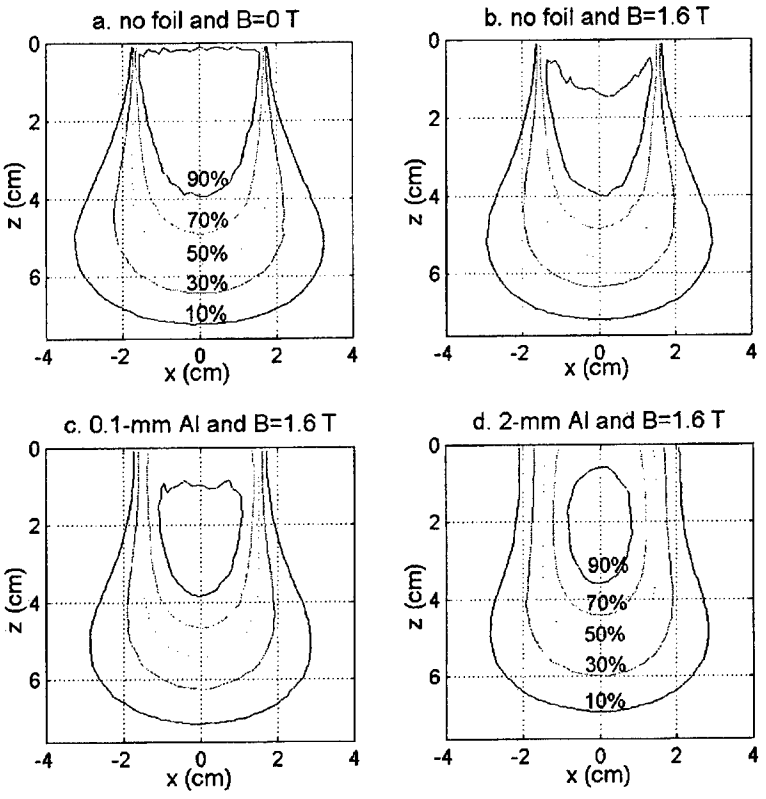

FIG. 3. Dose profiles for the 15 MeV electron beams: (a) without magnetic field collimation and foil attenuation, (b) with magnetic field collimation (1.6 T) and no foil attenuation, (c) with magnetic field collimation (1.6 T) and thin foil (0.1 mm Al) attenuation, and (d) with magnetic field collimation (1.6 T) and thick foil (2 mm Al) attenuation.

target, D_N is the dose to the sparing structure if specified, (x_i,z_i) is the grid point on the target boundary, w_i is the beam weighting factor, and α is a penalty parameter ranging from 0 to 1. The grid size for the calculation was set to 0.2 cm. The incident beam energy and the foil size were selected automatically based on the central axis depth profiles for every iterative location of the pencil beam. In Eq. (4), D_T and D_N depend on the beam energy and the foil thickness. The optimization parameters include beam energies, foil thickness, beam weights, and locations of the beams. Because the gradient can be computed analytically from Eq. (4), we adopted the multidimensional conjugate gradient optimization method. The optimization was performed in the MATLAB programming language.

Using Eqs. (3) and (4), we performed dose optimization for the simulated cases. In each calculation, multiple magnetically collimated pencil beams are placed across the treatment field. The incident beam energies vary from three to six values (6–18 MeV) depending on the maximum depth of the target. The simulated targets included a rectangle and a horseshoe shape. We fixed the reference depth for each magnetically collimated pencil beam. This allowed us to present the combined dose in arbitrary units and normalized to the same depth on the central beam axis. For each beam's energy, we selected Al foils of thickness 0–0.2 cm with a resolution of 0.05 cm. The goal was to allow 80% isodose line cover the whole target volume.

Next, we investigated the feasibility of generating an en-

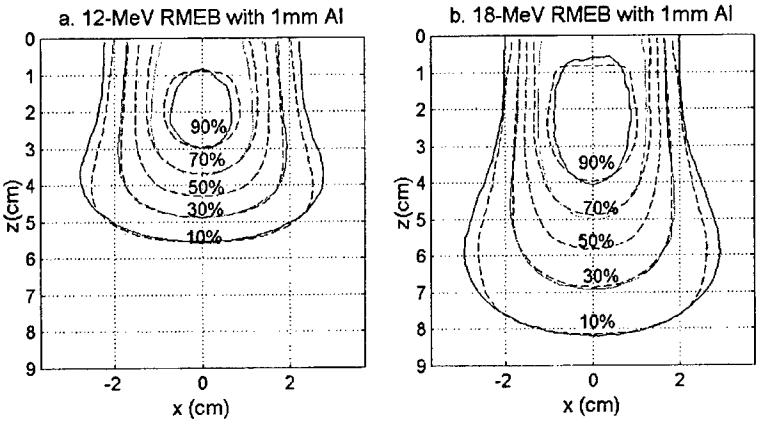

FIG. 4. Comparison of extended pencil beam dose model calculations (dashed lines) and Monte Carlo calculations (solid lines) of the 12 and 18 MeV magnetically collimated electrons with 0.1 cm Al foil attenuation.

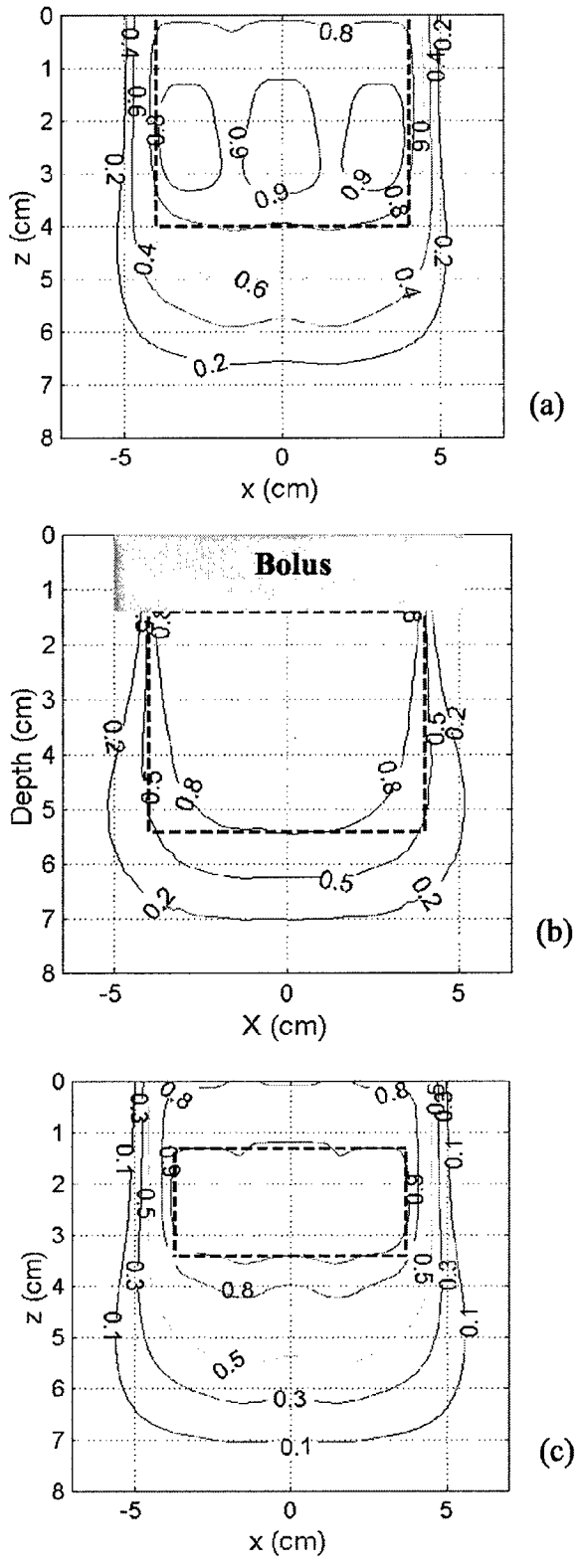

FIG. 5. Dose distributions for a rectangular target: (a) the optimized dose distribution where the 80% isodose line covers the target area, (b) the dose distribution using conventional 15 MeV electron beam and 1.4 cm bolus on the surface, and (c) the optimized dose distribution with RMEBs for the same target of (b).

TABLE II. The optimized beam parameters for the cases of simulated targets.

Target	Energy (MeV)	Foil (cm)	Weight	Position
Rectangle	15	0.1	0.958	−3.12
	15	0.1	0.963	0
	15	0.2	0.958	3.12
Horseshoe	18	0.2	0.980	−3.90
	9	0.2	0.483	−2.01
	9	0.2	0.310	−0.70
	9	0.2	0.310	0.70
	9	0.2	0.483	2.01
	18	0.2	0.980	3.90

hanced electron depth dose distribution by mixing magnetically collimated electron beams through metal foil modulation. This technique is analogous to the technique of producing spread-out Bragg peak in proton therapy. The maximum electron energy of 30 MeV was selected for an adequate range of travel. Based on Eq. (1), the magnetic field strength was increased to 2.8 T for 30 MeV electron beam. This magnetic field strength may require a large-size magnet to produce. In addition, we used the collimation field size of 10×10 cm^2 to accommodate lateral scatter of 30 MeV electrons. For the purpose of the study, we selected three electron energies of 10, 15, and 30 MeV to produce the spread-out depth dose enhancement peak. The beam weights were optimized to produce a uniform spread-out peak.

III. RESULTS

Figures 1(a) and 1(b) show the depth doses for the 9 and 18 MeV range-modulated electron beams, respectively, with and without magnetic field collimation. Since longitudinal magnetic fields do not affect the maximum energy of the electron beam, we used the metal foils to adjust its range of travel. We studied the attenuating foils of the following materials: Al, Be, Cu, Pb, and Ti. The depth dose curves of Fig. 1 were normalized to the dose at the surface. The effect of the depth dose enhancement was not satisfactory in the case of the Pb due to large attenuation and photon contamination. The depth doses for Al, Be, and Ti were similar in shape. The ranges of the electron beams were found to be in the following descending order: Be, Al, Ti, Cu, and Pb. The bremsstrahlung contribution was in reverse order with the Pb resulting in the largest contribution and Be resulting in the smallest contribution. Because of the bio-toxic nature of the Be foils, we choose Al foils for electron range modulation. The aluminum foils are inexpensive and readily available in uniform thickness.

The central-axis depth doses of the 9 and 18 MeV range and range modulated electron beam (RMEB) via Al foils of different thickness are shown in Fig. 2. The results for the central-axis depth dose without the application of the magnetic field and the attenuating foils are also provided for comparison. From the results of Fig. 2, the skin-sparing effect at first decreases with the increasing foil thickness and

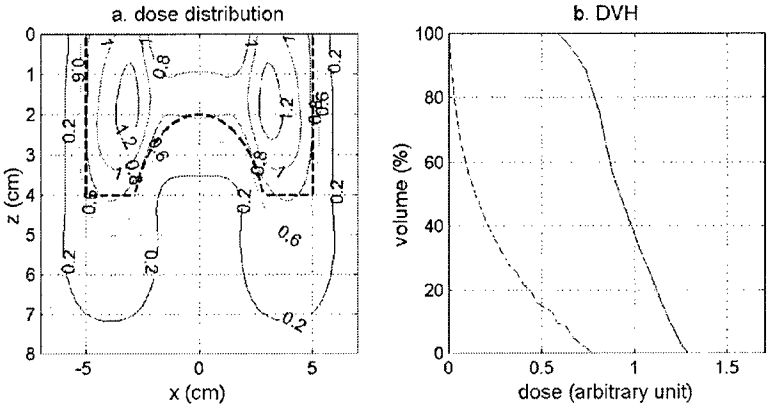

FIG. 6. Optimized dose distribution and DVH for the horseshoe-shaped target.

then increases again as the foils of more thickness are added. This is because the magnetic field is able to bend the electrons more to allow N_{rot} equal to multiples of 0.5 as the beam energy decreases with the increasing foil thickness. Overall, the D_{max} relative to the skin dose is 15%–40% higher for the RMEBs as compared with the conventional electron beams. This indicates that the selection of foil thickness and magnetic field strength will affect the depth-dose enhancement effect. From Fig. 2, the difference between the R_{50} values of a 0.01 and 0.2 cm Al foil is approximately 0.5 cm. This approximates the stopping power of electron in Al. From the results of Figs. 1 and 2, the shift in depth dose curve is typically more consistent with the changes in the foil thickness versus the atomic numbers.

The two-dimensional dose distribution of RMEBs as compared with the conventional electron beams is given in Fig. 3. Identical setup geometry was used for a conventional electron beam (15 MeV) and a RMEB. In Fig. 3, we compared the isodose distributions for the magnetically collimated electron beams with and without foils. It was found that the skin dose sparing is similar for both cases. The width of the penumbra at the surface increases for the beam with the foils. Since the magnetic field gyrates the peripheral electrons more toward the central axis, it reduces the beam divergence. This causes the beam penumbra to be less dependent on the depth of penetration as shown in Fig. 3. The metal foils further attenuate the peripheral electrons more than the central electrons because the peripheral transverse more thickness of foil due to divergence. As a result, the insertion of metal foils removes the "horns" of high isodose lines at the shallow depth as in Fig. 3. The extra scattering of the foils also slightly degraded the skin sparing (Fig. 1).

The results of the pencil-beam dose calculations are given in Fig. 4. The Monte Carlo calculations are also included. Overall, the two calculations agree within 0.2 cm. The main discrepancies occur in the low (<15%) and the high (>95%) isodose lines where the agreements are within 0.3 cm instead. This is mainly caused by the fluctuations in the transverse profiles at these depths when extracting the empirical parameters of the model.

The results of dose optimization for simple target geometries are shown in Fig. 5. In Fig. 5(a), a flat target of 8 cm long and 4 cm deep was outlined. The nominal beam energy and foil thickness were 15 MeV and 0.1 cm, respectively. The optimized parameters are listed in Table II. We compared the dose distributions of the same target using a single electron beam without magnetic collimation. To achieve similar depth penetration, we used a bolus of 1.4 cm for the conventional case, where the 80% isodose line along the central axis reaches the deepest extension of the target. The results are given in Fig. 5(b). The dose homogeneity is significantly worse for the single electron beam case particularly around the sharp corners of the target extension. We also adjusted the beam optimization parameters to allow the 90% isodose to cover a target situated below the surface. This is shown in Fig. 5(c). The resulting dose in the target is exceptionally uniform with less than 2% variations.

In Fig. 6, we show the optimization results for a horseshoe-shaped target. The circular region immediately below the arc region is treated as a critical structure. The dose distribution was optimized by combining six pencil beams of 9 and 18 MeV RMEBs. The DVHs for the target and the critical regions are plotted. The average dose for the target is

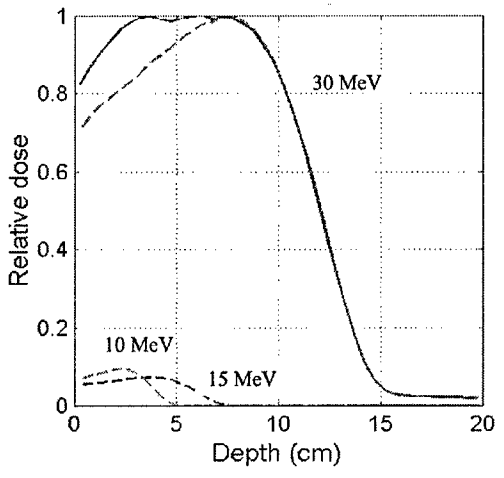

FIG. 7. A spread-out depth dose enhancement peak generated via magnetically collimated electron beams of 10, 15, and 30 MeV. Their relative contributions are plotted in the dashed lines.

94%±17% of the maximum dose. The resulting optimization parameters for the cases are given in Table II. The computational time is about 10 min on a Pentium IV 600 MHz personal computer for this case.

In Fig. 7, the results of a spread-out electron depth dose peak are presented. The beam weights for producing this uniform spread-out peak are 0.095 for 10 MeV, 0.074 for 15 MeV, and 1.000 for 30 MeV RMEB. The resulting dose is uniform across the spread-over peak with an average 99.3% of the maximum dose and a deviation of less than 1%. The skin dose for the spread-out peak is approximately 80% of the maximum dose. Despite improvement over the conventional electron beam of 30 MeV, the range straggling effect is significantly larger for the spread-out peak of the RMEBs as compared with a 5 cm SOBP produced from the proton beams.

IV. SUMMARY

We developed a method of using magnetic collimation together with metal foil modulation for producing range-modulated electron dose distributions. We investigated and demonstrated potential benefits of this approach, which include conformal electron dose distributions and enhanced spread-out depth dose peaks. Our study indicates that it is possible to use an external axial magnetic collimator in conjunction with metal foils to modulate electron beam dose distributions. Our ongoing work includes commissioning a magnetic collimator and an Al foils for beam-on measurements.

ACKNOWLEDGMENTS

We are indebted to our colleagues Dr. Matt Earl, Dr. Allen Li, Dr. Shahid Naqvi, Dr. Mehrdad Sarfaraz, Dr. David Shepard, Dr. Xingen Wu, and Dr. Cedric Yu for support. This work was supported in part by research grants from the Department of Defense and the University of Maryland School of Medicine.

[a]Author to whom correspondence should be addressed; electronic mail: Ima001@umaryland.edu

[1] M. A. Earl and L. Ma, "Depth dose enhancement of electron beams subject to external uniform longitudinal magnetic fields: A Monte Carlo study," Med. Phys. **29**, 484–91 (2002).

[2] F. J. Farley, G. Fiorentini, and D. C. Stocks, "Influence of axial magnetic field on the multiple scattering of particle beams," Nucl. Instrum. Methods **152**, 353–356 (1978).

[3] C. C. Shih, "High energy electron radiotherapy in a magnetic field," Med. Phys. **2**, 9–13 (1975).

[4] V. Y. Kuperman, "Electron beam transport in the presence of a strong, axial magnetic field," Med. Phys. **28**, 2522–2526 (2001).

[5] R. Nath and R. J. Schulz, "Modification of electron-beam dose distributions by transverse magnetic fields," Med. Phys. **5**, 226–230 (1978).

[6] B. R. Paliwal, A. L. Wiley, Jr., B. W. Wessels, and M. C. Choi, "Magnetic field modification of electron-beam dose distributions in inhomogeneous media," Med. Phys. **5**, 404–408 (1978).

[7] M. S. Weinhous, R. Nath, and R. J. Schulz, "Enhancement of electron beam dose distributions by longitudinal magnetic fields: Monte Carlo simulations and magnet system optimization," Med. Phys. **12**, 598–603 (1985).

[8] D. P. Whitmire, D. L. Bernard, M. D. Peterson, and J. A. Purdy, "Magnetic enhancement of electron dose distribution in a phantom," Med. Phys. **4**, 127–131 (1977).

[9] W. Bostick, "Possible techniques in direct-electron beam tumor therapy," Phys. Rev. **77**, 564 (1950).

[10] A. F. Bielajew, "The effect of strong longitudinal magnetic fields on dose deposition from electron and photon beams," Med. Phys. **20**, 1171–1179 (1993).

[11] M. C. Lee and C. M. Ma, "Monte Carlo characterization of clinical electron beams in transverse magnetic fields," Phys. Med. Biol. **45**, 2947–2967 (2000).

[12] D. W. Litzenberg, B. A. Fraass, D. L. McShan, T. W. O'Donnell, D. A. Roberts, F. D. Becchetti, A. F. Bielajew, and J. M. Moran, "An apparatus for applying strong longitudinal magnetic fields to clinical photon and electron beams," Phys. Med. Biol. **46**, N105–N115 (2001).

Depth dose enhancement of electron beams subject to external uniform longitudinal magnetic fields: A Monte Carlo study

M. A. Earl[a] and L. Ma
University of Maryland School of Medicine, Baltimore, Maryland 21201

(Received 25 September 2001; accepted for publication 7 January 2002; published 12 March 2002)

We studied the dose distributions from electron beams subjected to a longitudinal magnetic field applied to them before they reach the phantom. We found that specific combinations of the length and intensity of the magnetic field produced enhancement of the peaks of the central-axis depth-dose distributions. The EGS4 Monte Carlo system was used in this study. In the simulations, a uniform axial magnetic field parallel to the electron beam direction was applied to the air gap between the collimation and the phantom. We extensively studied the simplified case of an 18 MeV electron beam point source. Dose deposition was calculated for various magnetic field strengths, distances through which the magnetic field was applied, collimation sizes, and source to collimation distances. The magnetic field strengths varied from 0 to 3 T, the source-to-collimation distances studied were 50 and 95 cm, the collimation sizes studied were 10×10 and 20×20 cm^2, and the distance through which the field was applied ranged from 10 to 20 cm. Specific combinations of these variables resulted in as much as a 70% enhancement of the peak dose relative to the surface dose. Finally, to determine how the geometry of a real accelerator affects the resulting dose distribution, we performed a full simulation of an Elekta SL20 linear accelerator and compared the results with the ideal case. © *2002 American Association of Physicists in Medicine.*
[DOI: 10.1118/1.1461374]

I. INTRODUCTION

Electron beam radiotherapy is generally used to treat shallow lesions. For example, in the treatment of breast cancer, electrons are sometimes used as a boost treatment after surgery to eradicate any remaining microscopic disease. In spite of the benefits, electron beams often produce an undesirably high skin dose. In addition, the broadening of the penumbra with increasing depth can cause unwanted dose to critical structures and normal tissue around the lesion. In this work, we explore the possibility of applying magnetic fields to electron beams in order to alleviate these unwanted side-effects of electron therapy.

The use of longitudinal magnetic fields to alter the dose deposition characteristics of radiation beams used in cancer management has previously been investigated by several authors. Bostick first proposed the application of a magnetic field to an electron beam in order to enhance the dose deposition at increased depths and to reduce the penumbra broadening with depth.[1] Weinhous *et al.* performed a Monte Carlo study of the application of a longitudinal magnetic field to electron beams.[2] The purpose of this study was to test the feasibility of the magnet design and to determine the effects on the dose distribution from the magnetic field application. Bielajew later showed that application of strong longitudinal magnetic fields confines the dose deposition of both electron and photon beams.[3] For electrons, the field forces the electrons to spiral around the field lines, confining the dose deposition. For photons, the field limits the lateral spread of secondary electrons, effectively reducing the penumbra of the beam. Although the effect was clear, large magnet strengths of up to 20 T were required. Recently, Naqvi *et al.* proposed the application of magnetic fields with strengths on the order of 0.5 T on air cavities in order to control the loss of electronic equilibrium at the interface between high and low density media.[4]

Despite the numerous studies of the use of magnetic fields in radiotherapy, there has been little work on the possibility of application of the field in a region external to the phantom. With the exception of Sempert in 1960,[5] most authors investigated the application of the field directly to the phantom. It is this gap in the literature that has motivated this work. We report the results from a Monte Carlo study that investigated the effects of applying a magnetic field to an electron beam in the region immediately above the phantom surface.

We performed EGS4 Monte Carlo studies of electron beams subjected to a uniform longitudinal magnetic field applied to the air gap between the collimation and the surface of the phantom. Dependence on various parameters such as source-to-collimator distance, collimation size, length of the magnetic field, and magnetic field strengths were studied.

As charged particles traverse a magnetic field, they experience the Lorentz force $q\boldsymbol{v}\times\boldsymbol{B}$, where q is the charge of the particle, $\boldsymbol{v}$ is the velocity of the particle, and $\boldsymbol{B}$ is the magnetic field. The resulting trajectory is a helix about an axis parallel to the magnetic field whose gyration radius is given by

$$r_g=\frac{p_\perp}{3.0|\boldsymbol{B}|}, \tag{1}$$

where $p_\perp$ is the component of momentum perpendicular to the magnetic field lines in MeV/c (c is the speed of light in

 0094-2405/2002/29(4)/484/8/$19.00

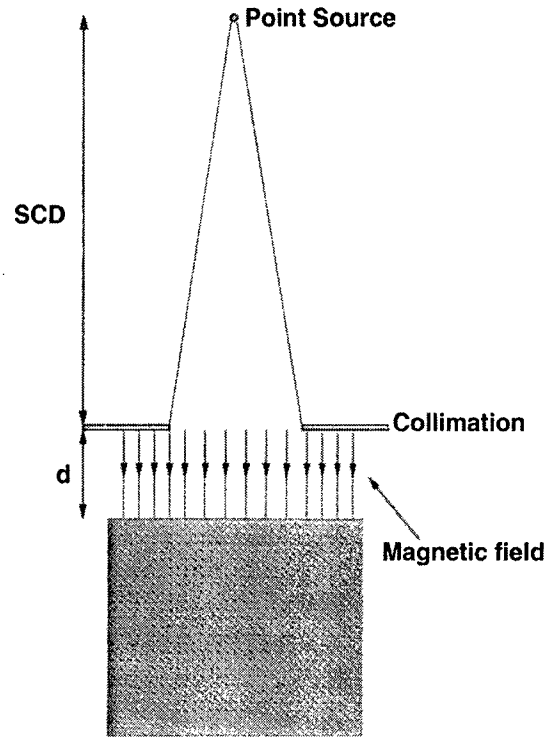

FIG. 1. Schematic of simple setup for Monte Carlo simulation.

vacuum), and $|B|$ is the magnetic field strength in tesla (T). The frequency with which electrons orbit in a magnetic field is given by

$$\omega_g = \frac{1}{\gamma}\omega^e_{\text{cycl}}|B|, \tag{2}$$

where $\gamma = 1 + T/(mc^2)$ is the Lorentz relativistic boost factor (T and m are the kinetic energy and rest mass of the particle, respectively), and ω^e_{cycl} is the electron cyclotron frequency which is a constant of nature and is approximately $\omega^e_{\text{cycl}} \approx 1.758\,82 \times 10^{11}\ \text{rad s}^{-1}\,\text{T}^{-1}$.

II. MATERIALS AND METHODS

We used the EGS4 Monte Carlo system[6] in this study. Dose deposition was calculated for electron beams subjected to uniform magnetic fields applied in a region external to the phantom. In particular, we used a version of the DOSXYZ user code[7] modified by Ma to include the magnetic field module developed by Bielajew.[3] The tracking algorithm of electrons in electromagnetic fields is outlined in Ref. 8.

The default PRESTA algorithm[9] was used for electron transport in the simulation from which the values for ESTEPE were determined. The cutoff energy for electrons (ECUT) was set to 600 keV and that for photons (PCUT) was set to 10 keV in all simulations.

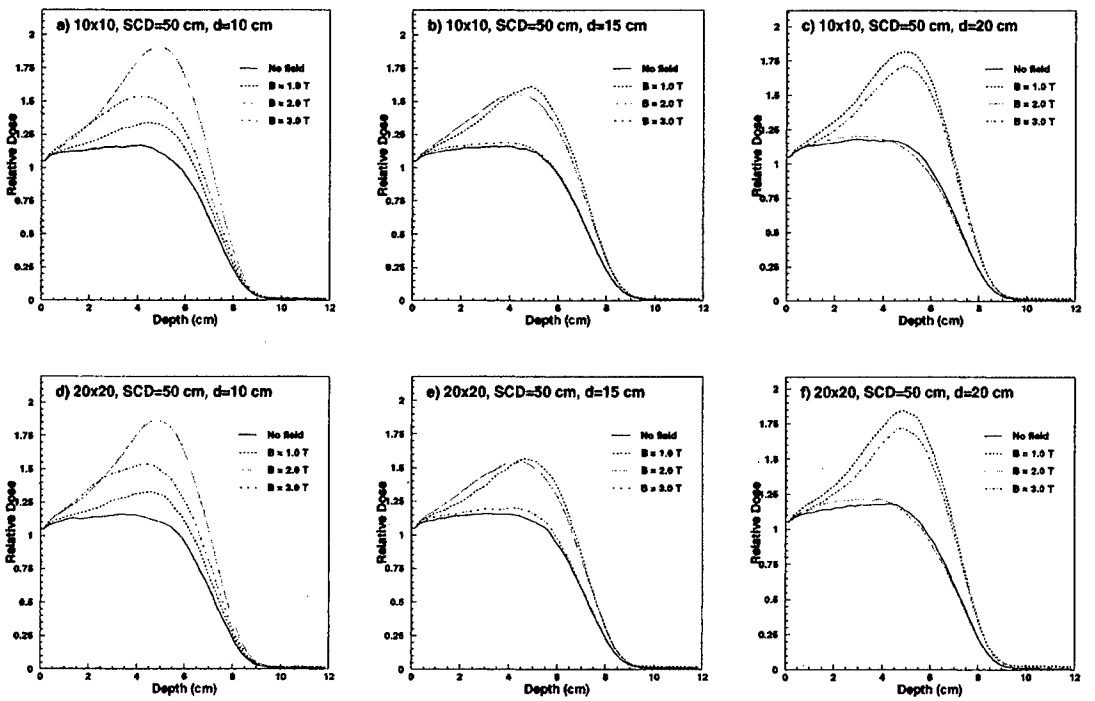

FIG. 2. Depth dose profiles for the simulation geometry depicted in Fig. 1. An 18 MeV electron point source with 50 cm SCD subject to magnetic field strengths of 0, 1, 2, and 3 T. The source was not monoenergetic, but derived from a spectrum calculated using the EGS4 BEAM user code. (a)–(c) The result of 10×10 cm^2 collimation. (d)–(f) The result of 20×20 cm^2 collimation. (a)/(d) $d=10$ cm, (b)/(e) $d=15$ cm, (c)/(f) $d=20$ cm. All profiles were normalized to the dose near the surface (depth of 0.25 cm).

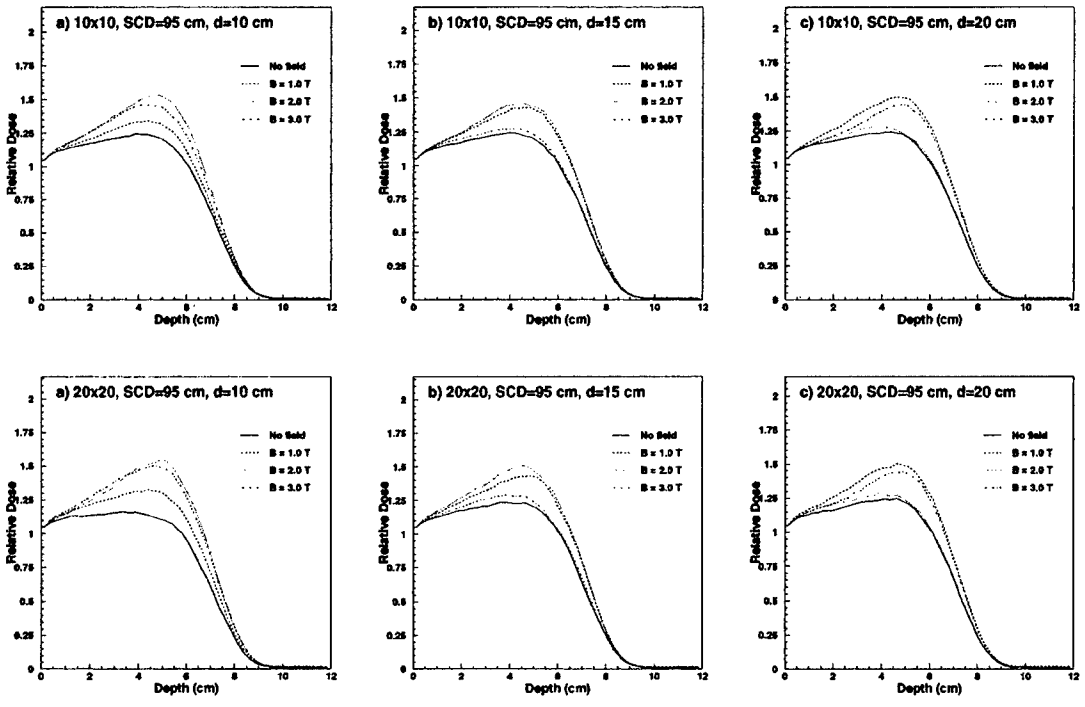

FIG. 3. The same as Fig. 2 except SCD=95 cm.

A simplified geometry was used to study the dependence of the depth dose distribution on several parameters: collimation size, the source-to-collimation distance (SCD), the distance d through which the field was applied, and the magnetic field strengths $|\boldsymbol{B}|$. The setup geometry and these parameters are illustrated in Fig. 1. The collimation was infinitesimally thin and had zero transmission. We studied collimation sizes of 10×10 and 20×20 cm^2, SCDs of 50 and 95 cm, d's of 10, 15, and 20 cm, and $|\boldsymbol{B}|$'s of 0, 1, 2, and 3 T. A Monte Carlo calculation with an 18 MeV electron point source was performed for each combination of these parameters. The 18 MeV electron beam was not monoenergetic but sampled from a spectral distribution of an 18 MeV electron beam calculated using the BEAM user code.[10,11]

Since the magnetic field module is part of the DOSXYZ user code, the magnetic fields must be confined to the geometry specified in the DOSXYZ input file. Immediately below the collimation is the DOSXYZ phantom consisting of an air gap to which $\boldsymbol{B}$ is applied, followed by a water region in which dose is scored. The voxel size was set to 0.125 cm in the high-gradient penumbra region, and to 0.5 cm in the flat part of the field. The voxel size in the z direction was set to be 0.2 cm.

Finally, to investigate the effects of real accelerator head geometry, we performed a study using phase space files generated with the BEAM user code from NRCC.[10,11] The phase space files that we created contain the positions and momenta of the electrons and photons from electron beams generated by an Elekta SL20 linear accelerator. The files realistically model the geometry of the accelerator head in order to account for effects such as head scatter. We used the final phase space files as input to the dose calculation for a selected number of cases. These results were then compared to those from the point source calculation to determine the effects due to a real accelerator geometry. In addition, the phase space files were used to calculate the energy spectrum of an 18 MeV electron beam. It is this spectrum from which we sampled in the point source calculations described previously.

III. RESULTS AND DISCUSSION

A. Idealized geometry

In this section, we describe the results of the simulations which used the geometry depicted in Fig. 1. A variety of central-axis depth dose distributions are shown in Figs. 2 and 3 for SCDs of 50 and 95 cm, respectively. Each individual figure shows all magnetic field strengths for a specific configuration of SCD, d, and field size. The most significant result is the enhancement in peak dose relative to the surface dose.

There is little variation with field size, as seen from the 10×10 and 20×20 cm^2 cases. However, there is a significant

TABLE I. A summary of the number of rotations N_{rot} an electron undergoes while subjected to a uniform magnetic field of strength B and distance that it traversed the field d.

B field (T)	d=10 cm	d=15 cm	d=20 cm
1	0.265	0.397	0.530
2	0.530	0.794	1.060
3	0.794	1.191	1.628

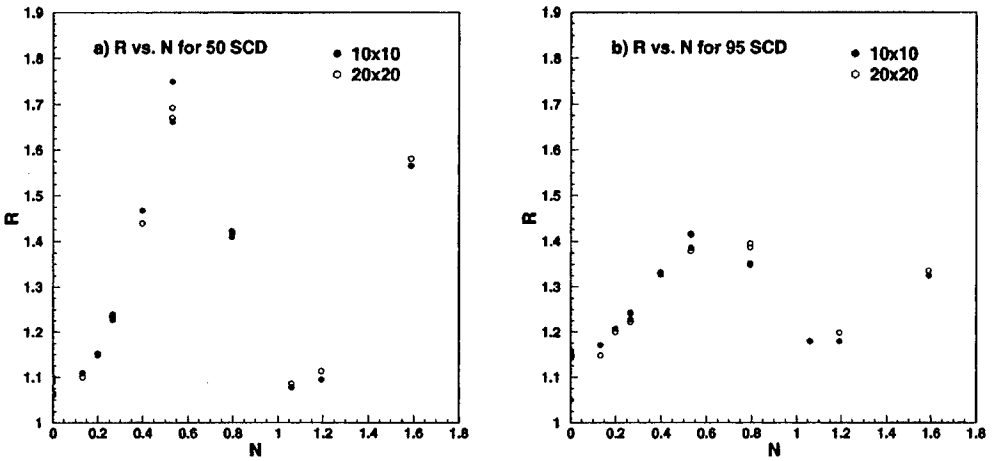

FIG. 4. Dose enhancement variable R_{pdd} as a function of N_{rot} for (a) SCD=50 cm and (b) SCD=95 cm.

dependence on d. For instance, in Figs. 2(a) and 2(c) (the case of $d=10$ cm) the enhancement is maximized when $B=2.0$ T. However, in Figs. 2(c) and 2(f) (the case of $d=20$ cm), the enhancement is maximized when $B=1.0$ T. In fact, for this case the enhancement effectively disappears for $B=2.0$ T.

To quantify the dose enhancement, we define a ratio R_{pdd},

$$R_{pdd}=\frac{D(x=x_{ref})}{D(x=x_{surf})}, \tag{3}$$

where $D(x)$ is dose along the central axis at a depth x, x_{ref} is a reference depth, and x_{surf} is a depth near the surface. For the our study, we took x_{surf} to be 0.25 cm. For most of the distributions the maximum was close to 4.5 cm, so we set x_{ref} to this value.

In order to better understand the effect, we studied R_{pdd} as a function of N_{rot}, where N_{rot} is the number of rotations the electron undergoes while in the magnetic field and is given by

$$N_{rot}=\frac{\omega_g t}{2\pi}, \tag{4}$$

where ω_g is given in Eq. (2) and t is the amount of time the electron spends in the field. This can be written as

$$t=\frac{d}{\beta_{\|} v}, \tag{5}$$

where $\beta_{\|}$ is the electron's component of velocity parallel to the beam axis relative to its absolute velocity and v is the absolute velocity of the electron. Since the electrons are highly relativistic, v can be taken to be the speed of light in a vacuum c. The relativistic expression $\beta=p/E$ can then be used to write $\beta_{\|}$ as

$$\beta_{\|}=\frac{p_{\|} c}{E}, \tag{6}$$

where $p_{\|}$ is the electron's component of momentum parallel to the beam axis. This can be written as

$$p_{\|}=|\boldsymbol{p}|\cos\theta, \tag{7}$$

where θ is the angle the momentum vector makes with the central axis. Combining Eqs. (2), (4)–(6), and (7) we arrive at an expression for N_{rot},

$$N_{rot}=\frac{1}{2\pi}\frac{|\boldsymbol{B}|d(T+mc^2)}{\gamma|\boldsymbol{p}|c^2\cos\theta}\omega^e_{cycl}. \tag{8}$$

By making the following approximations:

$$T+mc^2\approx|\boldsymbol{p}|c, \tag{9}$$

$$\cos\theta\approx 1, \tag{10}$$

the expression for N_{rot} is reduced to

$$N_{rot}\approx\frac{1}{2\pi}\frac{|\boldsymbol{B}|d}{\gamma c}\omega^e_{cycl}. \tag{11}$$

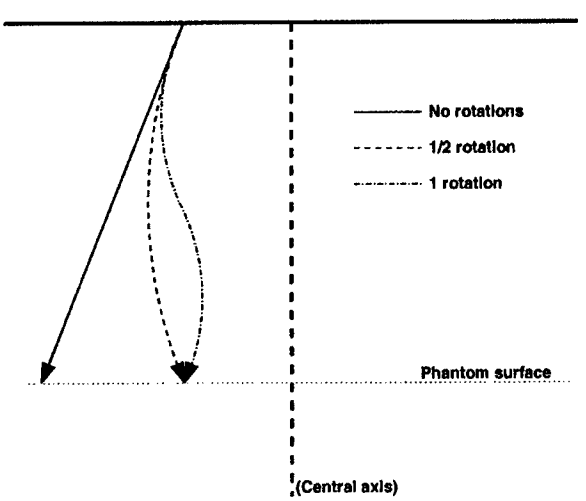

FIG. 5. Illustration of focusing effect. With no magnetic field application, electrons are always directed away from the central axis (solid line). With magnetic field applied so that electrons undergo 1/2 a rotation, electrons are always directed toward the central axis (dashed line). With magnetic field applied so that electrons undergo a full rotation, electrons are directed away from the central axis, but are spatially closer to the central axis (dash-dot line).

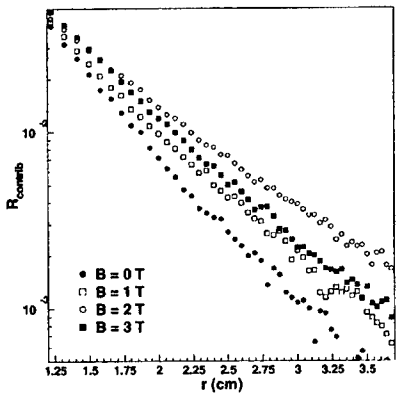

FIG. 6. R_{contrib} as a function of distance of annulus from the central axis.

N_{rot} is linearly proportional to the $|\boldsymbol{B}|d$ product and inversely proportional to γ. Table I summarizes the number of rotations for all configurations. The values in Table I were calculated by setting $\gamma=(18\text{ MeV})/(0.511\text{ MeV})\approx 35$.

Figures 4(a) and 4(b) show R_{pdd} versus N_{rot} for 50 and 95 cm SCD, respectively. The dependence of R_{pdd} on N_{rot} is not linear but is periodic. The maximum enhancement occurs when the electrons undergo 1/2 of a rotation while the enhancement is minimized when they undergo a full rotation. This is most likely due to a focusing effect. For no magnetic field, the component of momentum perpendicular to the central axis of the beam is always directed away from the central axis. However, if a magnetic field is applied in such a way that the electrons undergo $n+\frac{1}{2}$ of a revolution (where n is an integer $=0,1,2,...$), the perpendicular component is directed into the central axis. Therefore, electrons striking the surface of the phantom away from the center of the field contribute more to dose along the central axis at larger depths. This focusing effect is illustrated in Fig. 5. We should also note that the decrease in R_{pdd} for 95 cm SCD relative to 50 cm SCD is due to a smaller perpendicular component of momentum for an equivalent geometrical position in the field. In other words, for 95 cm SCD, the electrons are directed inward at a smaller angle relative to the central axis.

To verify the focusing effect, we studied a 10×10 cm^2 field at 50 cm SCD in detail. The field was divided into 100 equi-area rectangular "annuli" emanating from the center of the field. The dose was scored for each "annulus" to determine the contribution to dose at the central axis from each. In theory, cases of $n+\frac{1}{2}$ revolution will have annuli further away from the center of the field contributing more to central-axis dose than the case in which $|\boldsymbol{B}|=0$.

In order to quantify this, we define a new ratio R_{contrib} as

$$R_{\text{contrib}}=\frac{D_i(x=x_{\text{ref}})}{D_{\text{tot}}(x=x_{\text{ref}})}, \tag{12}$$

where $D_i(x)$ is the central-axis dose at depth x from the ith annulus. Once again the value of x_{ref} was taken to be 4.5 cm. In Fig. 6, we show R_{contrib} as a function of the distance r from the central axis for $|\boldsymbol{B}|=0$, 1, 2, and 3 T. For cases where the electrons undergo $n+\frac{1}{2}$ of a rotation, annuli further away from the center of the field have a higher value of R_{contrib} than the case of no magnetic field application. This evidence supports the focusing hypothesis.

Figure 6 shows a steady decrease of R_{contrib} for all cases, although for $|\boldsymbol{B}|=2.0$ T, it decreases more slowly than the others. Despite this, there is an end point of approximately $r=5$ cm where there is negligible contribution to the central-axis depth dose peak. This is the reason why increasing the field size to 20×20 cm^2 does not result in a higher value for R_{pdd}.

Although nearly ideal, the simulations described previously were not exactly ideal due to the spectral source and the air-filled interface region between the collimation and the water phantom. In order to study these effects, we performed three additional simulations for a case of 10×10 cm^2 field size, SCD=50 cm, and $d=10$ cm. The truly ideal case used an 18 MeV monoenergetic point source and had vacuum in the interface region. The other two cases were (a) 18 MeV monoenergetic with air in the interface region and (b) 18 MeV spectrum with vacuum in the interface region. For all of these simulations, we chose $|\boldsymbol{B}|=1.88$ T, the value that gives approximately one half of a rotation. The results of the simulations are shown in Figs. 7(a) and 7(b).

Figure 7(a) shows less than 2% degradation of the enhancement factor R_{pdd} due to the inclusion of air in the interface region. This slight degradation is because of the scattering of some electrons toward the central axis. Such electrons will then be directed away from the central axis after traversing the magnetic field.

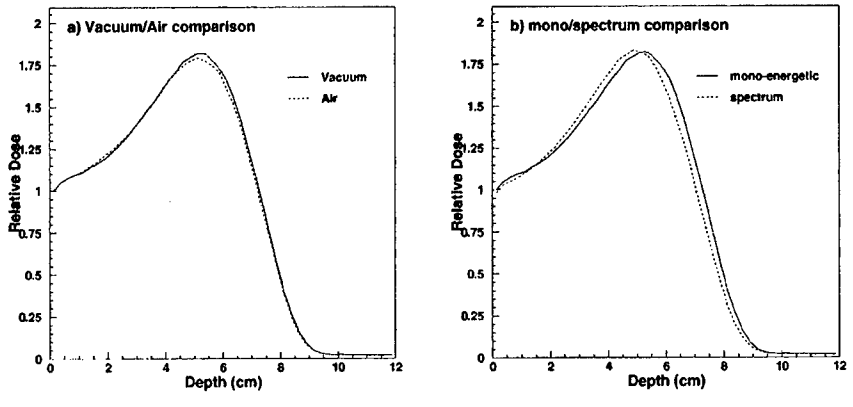

FIG. 7. Comparison of the (a) air effect and (b) spectral effect to the truly ideal case for 10×10 cm^2 field size, SCD=50 cm, and $d=10$ cm. A magnetic field strength of $|\boldsymbol{B}|=1.88$ T was used to produce exactly 1/2 of a rotation.

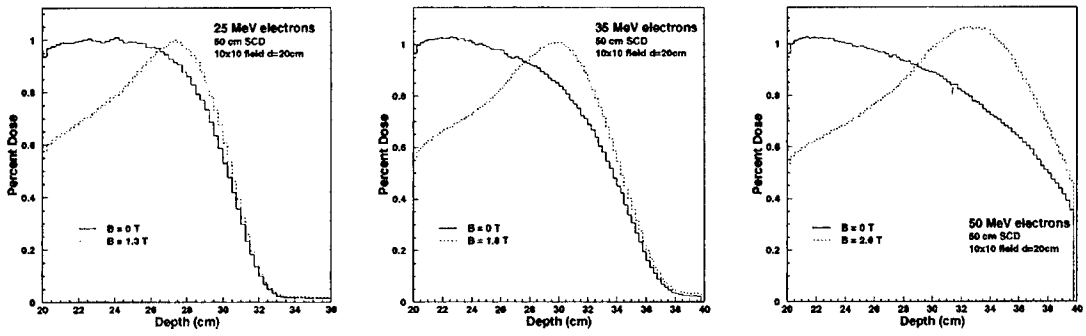

FIG. 8. Energy dependence of magnetic field induces dose enhancement. Values of R remain the same regardless of energy.

Figure 7(b) shows a minimal degradation of R_{pdd} due to the energy spectrum. This can be attributed to the fact that the spectrum has a narrow width of approximately 0.2 MeV. By calculating the differential

$$|\delta N_{\text{rot}}| = \frac{1}{2\pi}\frac{\delta E}{E}\frac{|\boldsymbol{B}|d}{\gamma c}\omega^{e}_{\text{cycl}}, \tag{13}$$

we get $|\delta N_{\text{rot}}| \approx 0.006$, or 2°. Despite the negligible degradation of R_{pdd} there was a slight shift in the peak dose. This can be attributed to the lower energy component of the energy spectrum.

We also studied the energy dependence of the dose enhancement. Simulations using monoenergetic 25, 35, and 50 MeV electron beams with 10×10 cm^2 field size, SCD=50 cm, $d=20$ cm, and $|\boldsymbol{B}|$ that produces roughly 1/2 a revolution (for each particular energy) were used as parameters in this study. We used $|\boldsymbol{B}| = 1.3$, 1.8, and 2.6 T for 25, 35, and 50 MeV beams, respectively. In addition, we ran the same simulations with no magnetic field applied. The results are shown in Fig. 8. The dose enhancement ratios for the three additional cases were 1.7, 1.8, and 1.8 as compared with a maximum of 1.7 for the 18 MeV case. No conclusive statement can therefore be made about the dependence of the enhancement on energy.

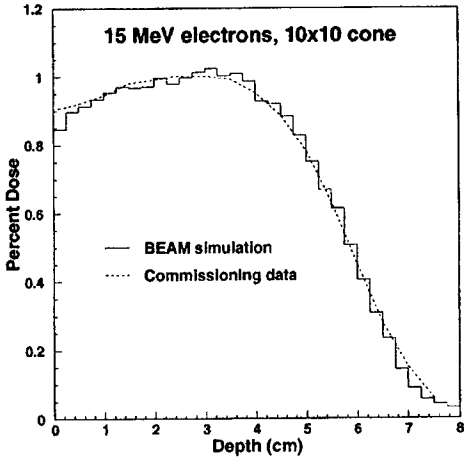

FIG. 9. Depth dose comparison of BEAM simulation and commissioning data for a 15 MeV electron beam with a 10×10 cm^2 applicator cone.

B. Realistic geometry

The results shown in Sec. III A are for an idealized case. We have not included the effects caused by the complicated geometry of the accelerator head.

In the previous results, we idealized the accelerator treatment head as a point source with perfect collimation below it. In order to study potential detrimental effects caused by a real linac geometry, we used the BEAM user code[10,11] to simulate the treatment head for an Elekta SL20 linear accelerator.

In the simulation of the treatment head, we included the various components such as the primary scattering foil, primary collimator, secondary scattering foil, ion chamber, X and Y diaphragms, and a 10×10 cm^2 applicator cone. Most of the specifications were provided by the vendor, but some parameters had to be tuned so that the depth dose and profile distributions from the simulation matched those from commissioning measurements. For instance, the incident electron energy and the openings of the X and Y diaphragms needed to be tuned. The accuracy did not need to be ideal, but had to give us an idea of how scattered electrons and contaminant photons affect the results. Figure 9 shows a comparison between the BEAM simulation and a commissioning measurement percent depth dose curves.

To check how accelerator treatment head effects can affect the results presented in Sec. III A, we ran a DOSXYZ simulation using the phase space data obtained from the BEAM simulation of an 18 MeV electron beam. Figure 10 is a schematic of the setup used. The distance from the source to the end of applicator cone was 95 cm and the cone size was 10×10 cm^2. We used $d=10$ cm and $|\boldsymbol{B}|=2$ T, a combination that produces $\approx 1/2$ a rotation. A comparison of the depth dose curves for the ideal case and the BEAM simulation is shown in Fig. 11. The dose enhancement is degraded by approximately 20% but does not disappear completely. This can be explained by the fact that a large percentage of electrons exiting the cone were unimpeded in the treatment head and therefore had momenta directed away from the central-axis when exiting the applicator cone.

IV. CONCLUSION

The application of a longitudinal magnetic field to a region external to the phantom enhances the dose at the peak

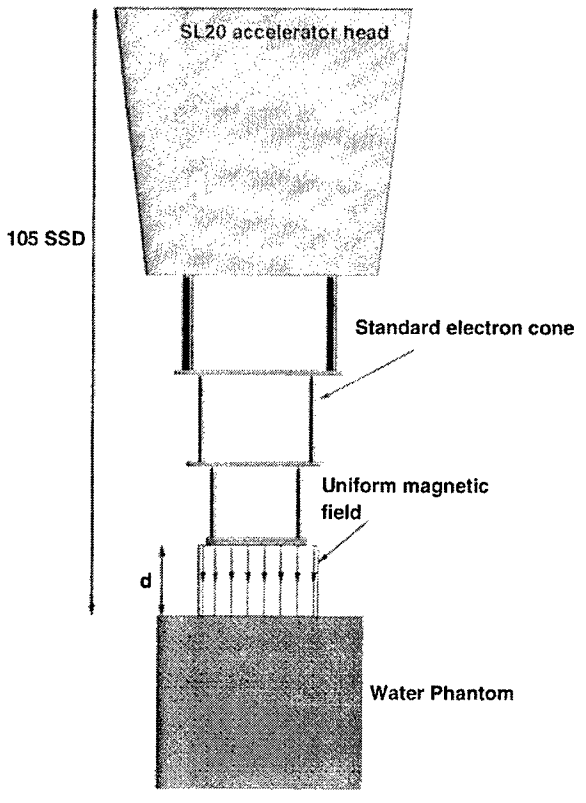

FIG. 10. Schematic of setup for simulations taking into account real accelerator effects.

relative to the dose near the surface. The effect is caused by the redirection of the momentum inward toward the beam axis. By undergoing a rotation of odd multiples of π, the effect is maximized while even multiples of π minimize the effect. The effect is therefore periodic. Because the peak is enhanced, this has implications of skin sparing in the treatment of shallow lesions.

In comparison with previous studies where the magnetic field was applied to the phantom, this work demonstrates that a more significant depth dose peak enhancement can be achieved with a comparable magnetic field strength. For example, Bielajew showed a 15% enhancement for a case of 20 MeV electrons with 50 cm SSD and application of a 3 T magnetic field.[3] Our enhancement for 18 MeV and the application of a 2 T magnetic field is approximately 60%–70%. The effect of the magnetic field is more significant in low-density media (air or vacuum) than high density media, like water, because of the dominance of deflections caused by multiple scattering in the latter case.

Since the dose enhancement effect is dependent on N_{rot}, it can be maximized by choosing appropriate values of d, $|\boldsymbol{B}|$, and the electron energy. Appropriate values for these parameters should be chosen when designing an apparatus. Other considerations should also be taken into account because of the relatively large $|\boldsymbol{B}|$ field strengths. For instance, Litzenberg *et al.* found unexpected effects when using a magnet with a large strength due to the fringing of the magnetic field lines.[12] The beam optics of linear accelerators can be significantly altered. Therefore, appropriate shielding of the fringe field must be studied. In addition, the fringe field will affect the trajectories of the electrons. These effects must be taken into account when designing a magnet and will be the subject of future work.

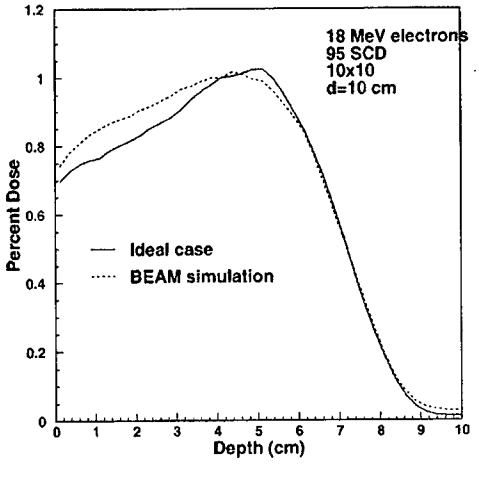

FIG. 11. Depth dose comparison of the two simulations whose setups are shown in Figs. 1 and 10.

ACKNOWLEDGMENTS

The authors would like to thank X. Allen Li for his assistance in running the Monte Carlo simulations. This work was supported by U.S. Army Research Grant No. BC99087.

[a]Author to whom all correspondence should be addressed; electronic mail: mearl001@umaryland.edu

[1] W. H. Bostick, "Possible techniques in direct-electron beam tumor therapy," Phys. Rev. **77**, 564 (1950).

[2] M. S. Weinhous, R. Nath, and R. J. Shultz, "Enhancement of electron beam dose distributions by longitudinal magnetic fields: Monte Carlo simulations and magnet system optimization," Med. Phys. **12**, 598–603 (1985).

[3] A. F. Bielajew, "The effect of strong longitudinal magnetic fields on dose deposition from electron and photon beams," Med. Phys. **20**, 1171–1179 (1993).

[4] S. A. Naqvi, X. A. Li, S. W. Ramahi, J. C. Chu, and S. Ye, "Reducing loss in lateral charged-particle equilibrium due to air cavities present in x-ray irradiated media by using longitudinal magnetic fields," Med. Phys. **28**, 603–611 (2001).

[5] M. Sempert, "New developments in high energy electron beam therapy with the 35 MeV Brown Boveri betatron," Radiology **7**, 105–106 (1960).

[6] W. R. Nelson, H. Hirayama, and D. W. O. Rogers, "The EGS4 code system," Stanford Linear Accelerator Center Report No. SLAC-265, SLAC, Stanford, CA, 1985.

[7] C.-M. Ma, D. W. O. Rogers, and B. Walters, "DOSXYZ Users Manual," National Research Council of Canada Report No. PIRS-0509B (revC), NRCC, Ottawa, Canada, 1998.

[8] A. F. Bielajew, "Electron transport in E and B fields," in *Monte Carlo Transport of Electrons and Photons*, edited by T. E. Jenkins, W. R. Nelson, A. Rindi, A. E. Nahum, and D. W. O. Rogers (Plenum, New York, 1987), pp. 421–434.

[9] A. F. Bielajew and D. W. O. Rogers, "PRESTA: The parameter reduced electron-step transport algorithm for electron Monte Carlo transport," Nucl. Instrum. Methods Phys. Res. B **18**, 161–181 (1987).

[10] D. W. O. Rogers, B. A. Faddegon, G. X. Ding, C.-M. Ma, and J. We-,"BEAM: A Monte Carlo code to simulate radiotherapy treatment units," Med. Phys. **22**, 503–525 (1995).
[11] D. W. O. Rogers, C.-M. Ma, B. Walters, G. X. Ding, D. Sheikh-Bagheri, and G. Zhang, "BEAM99 Users Manual," National Research Council of Canada Report No. PIRS-0509B (revD), NRCC, Ottawa, Canada, 1999.
[12] D. W. Litzenberg, B. A. Fraass, D. L. McShan, T. W. O'Donnell, D. A. Roberts, F. D. Becchetti, A. F. Bielajew, and J. M. Moran, "An apparatus for applying strong longitudinal magnetic fields to clinical photon and electron beams," Phys. Med. Biol. **46**, N105–115 (2001).